J. Fluid Mech. (2011), *vol.* 674, *pp.* 244–280.
doi:10.1017/S002211201000652X

Stirring, stretching and transport generated by a pair of like-signed vortices

F. RIZZI[1]† AND L. CORTELEZZI[2]‡

[1]Department of Physics, University of Udine, 33100 Udine, Italy

[2]Department of Mechanical Engineering, McGill University, Montreal, Quebec H3A 2K6, Canada

(Received 21 December 2009; revised 2 October 2010; accepted 18 December 2010; first published online 30 March 2011)

We consider a pair of like-signed, initially elliptical vortices with uniform vorticity distribution embedded in an incompressible, inviscid fluid occupying a two-dimensional, infinite domain. We characterize this finite-time, aperiodic, dynamical system in terms of its fixed points and separatrices, which divide the flow into inner core, inner recirculation, outer recirculation regions and outer flow. We numerically simulate the time evolution of the vortex pair using a contour dynamics algorithm. The rotational and co-rotational motion of the vortices perturb the separatrices, which undergo to deformations, yielding a tangle whose complexity increases as the amplitude of the perturbation increases. We analyse the dynamics of the tangle and explain the transport of fluid between different regions. We use two diagnostics to quantify stirring: stretching of the interface and the mix-norm. These two diagnostics characterize stirring in contradicting ways and present different sensitivity to the parameters considered. We find that stretching is dominated by the chaotic advection induced within the inner core and inner recirculation regions, whereas the mix-norm is dominated by the laminar transport induced within the outer recirculation regions. For pairs of vortices of small aspect ratio, stretching is piecewise linear and the mix-norm does not decrease monotonically. We show that these two effects are strongly coupled and synchronized with the rotational motion of the vortices. Since the nominal domain is unbounded, we quantify stirring on three concentric, circular domains. One domain nearly encloses the outer separatrices of the vortex pair, one is smaller and one larger than the first one. We show that the mix-norm is very sensitive to the size of the domain, while stretching is not. To quantify the sensitivity of stirring to the geometry of the initial concentration field, we consider, as an initial scalar field, two concentrations delimited by a straight-line interface of adjustable orientation. We show that the interface passing through the centroids of the vortices is the one most efficiently stretched, while the initial concentration field with an orthogonal interface is the most efficiently stirred. Finally, we investigate the effects of the angular impulse on the stirring performance of the vortex pair. Stretching is very sensitive to the angular impulse, while the mix-norm is not. We show that there is a value of the angular impulse which maximizes stretching and argue that this is due to two competing mechanisms.

Key words: mixing, nonlinear dynamical systems, vortex flows

---

† Present address: Department of Mechanical Engineering, The Johns Hopkins University, Baltimore, MD 21218, USA.

‡ Email address for correspondence: crtlz@cim.mcgill.ca

1. Introduction

Transport and mixing of two or more fluids is widely encountered in nature, for instance in atmospheric and oceanic phenomena, and also constitutes a key mechanism in many industrial applications involving combustion or chemical reactions, and pharmaceutical and food-industry processes, to name a few. Mixing results from the coupling of advective and diffusive mechanisms and can be broadly categorized according to the regime of the underlying flow: laminar or turbulent mixing. In general, turbulent flows have an excellent mixing performance with respect to laminar flows where transport is non-chaotic.

Turbulent mixing can be viewed as a three-stage process (Eckart 1948), comprised of entrainment, stirring and diffusion, spanning the full spectrum of space–time scales of the flow. It has been widely studied both theoretically and experimentally (see, to name a few, Leonard & Hill 1992; Flohr & Vassilicos 1997; Poje & Haller 1999; Slessor, Bond & Dimotakis 1998; Warhaft 2000; Dimotakis 2001; Smyth, Moum & Caldwell 2001; Vassilicos 2002; Meunier & Villermaux 2003; Villermaux & Duplat 2003; Dimotakis 2005; Aguirre, Nathman & Catrakis 2006; Sau & Mahesh 2007; Shadden *et al.* 2007; Deneve, Fröhlich & Bockhorn 2009 and references therein). The main mechanism underlying turbulent flows is the evolution and mutual interaction of vortical structures. Of particular interest are the coherent vortical structures identifiable at large scales of many turbulent flows of practical relevance, such as mixing layers, jets and wakes. A coherent structure can be thought of as a region of concentrated vorticity that retains its identity for long times (see e.g. Provenzale 1999), or as a set of fluid particles with distinct statistical properties (see e.g. Elhmaidi, Provenzale & Babiano 1993).

In many quasi-two-dimensional flows of interest, the evolution of coherent vortical structures can be modelled using pairwise interactions of vortices. This approach has been widely used to study the physical mechanisms responsible for vortex pairing and merging in two-dimensional turbulence (see e.g. Dritschel 1985; Melander, Zabusky & Styczek 1986; Melander, Zabusky & McWilliams 1988; McWilliams 1990; Dritschel & Zabusky 1996; Yasuda 1997; Von Hardenberg *et al.* 2000; Fuentes 2001; Rasmussen, Nielsen & Naulin 2001; Le Dizes & Verga 2002; Cerretelli & Williamson 2003*a*,*b*; Fuentes 2005; Huang 2005; Meunier, Le Dizès & Leweke 2005; Josserand & Rossi 2007; Sau & Mahesh 2007; Nybelen & Paoli 2009). On the other hand, mixing induced by pairwise interactions of vortices has received, in comparison, less attention (Witt *et al.* 1999; Estevadeordal & Kleis 2002).

To better understand transport and mixing in quasi-two-dimensional turbulence, it is important to characterize the dynamics of a pair of interacting vortices. We confine our interest to a pair of like-signed, identical, initially elliptic vortices during the phase of the evolution previous to merging. The dissipative effects are negligible during this phase (Cerretelli & Williamson 2003*a*); therefore, we analyse entrainment and stirring only, two of the three stages proposed by Eckart (1948). We neglect diffusion and model the vortex system with a pair of Kirchhoff vortices, i.e. a pair of vortex patches of uniform vorticity distribution, embedded in an incompressible, inviscid fluid occupying a two-dimensional, infinite domain. This vortex system is a finite-time, aperiodic dynamical system. We numerically describe the time evolution of the patches via contour dynamics (see Zabusky, Hughes & Roberts 1979; Pullin 1992 and references therein). Since the evolution of a pair of identical, like-signed vortices has radial symmetry, we characterize the performance of the vortex system on a circular domain and save computational time by imposing symmetry. The goal of this study is to characterize stirring, stretching and transport induced by a pair of initially elliptic vortices and identify the physical mechanisms behind it. This task is made difficult by the aperiodicity and finite timeness of the vortex system, and by the unboundedness of the domain.

We use dynamical system techniques to analyse the vortex system (e.g. Aref 1984; Khakhar, Rising & Ottino 1986; Leonard, Rom-Kedar & Wiggins 1987; Wiggins 1987; Ottino 1989; Rom-Kedar & Wiggins 1990, 1991; Rom-Kedar, Leonard & Wiggins 1990; Rom-Kedar *et al.* 1990; Beigie, Leonard & Wiggins 1991, 1994; Fuentes 2001, 2005 and references therein). Many studies have shown the importance of computing the invariant manifolds to describe transport, stretching and stirring of fluid particles under chaotic advection. In particular, the intersections of the invariant manifolds provide insight into how to partition a flow in regions of qualitatively different fluid motion and, subsequently, analyse the dynamics of the manifolds to explain the transport and stirring of fluid. In this study, however, we are limited by the finite timeness and aperiodicity of the system on the use of asymptotic techniques, such as Poincaré maps. Therefore, to overcome this difficulty and provide a reliable analysis, we resort to the use of a combination of diagnostics: tangle dynamics, finite-time Lyapunov exponents and direct expansion rate (see, e.g., Franjione & Ottino 1987; Rom-Kedar *et al.* 1990; Haller 2001; Padberg *et al.* 2009).

The unboundedness of the domain is also a source of difficulties for the quantification of mixing, stretching and transport, an issue that has been rarely addressed. In general, two characteristic lengths are necessary to characterize mixing. One is the largest scale over which mixing should be induced, and the other is the smallest scale mixing should target. As has been shown by Mathew, Mezic & Petzold (2005), mixing should be quantified accounting for the contribution at all scales, from the largest to the smallest. For bounded systems, the largest characteristic scale is usually dictated by the geometry of the domain. The matter is very different for unbounded, simply connected domains, where no characteristic length can be deduced from the geometry of the problem.

In this study we obtain a characteristic length, appropriate for quantifying stirring, stretching and transport, by describing the vortex system in terms of its fixed points and separatrices. The separatrices divide the fluid domain into four qualitatively different regions: the inner core regions, the inner recirculation region, the outer recirculation regions and the outer flow (Cerretelli & Williamson 2003*a*). The outer separatrices, which enclose the first three regions, identify a nearly circular domain surrounded by the outer flow. The radius of this domain is the largest length scale over which stirring should be quantified. As the vortex system evolves, the system of separatrices deforms but remains within the circular domain, and the transport of fluid in and out of the domain is negligible.

Owing to the mutual interaction of the vortex patches, the initial velocity field is perturbed by the rotational and co-rotational motion of the patches, and the strength of the perturbations depends on the aspect ratio of the initially elliptic vortices. To characterize the transport induced by the vortex system, we compute the manifolds of the fixed points of the flow. We characterize the tangle dynamics by identifying the fluid enclosed in each region (inner core, inner recirculation, outer recirculation and outer flow) with a different colour. Lobe dynamics allows us to analyse how the colour-coded fluid is stirred and transported under the effect of the perturbations.

To quantify stirring and its sensitivity to the size of the domain, we consider three concentric, circular domains. One domain nearly encloses the outer separatrices, one is about 14 times smaller and one is about three times larger than the first one.

To quantify the sensitivity of stirring to the geometry of the initial concentration field, we consider as an initial scalar field a simple configuration where two different concentrations are delimited by a straight-line interface of adjustable orientation. We use two diagnostics to characterize stirring: stretching of the interface and the mix-norm. The time evolution of stretching, or the number of lamellae, is a classical diagnostic, which has been used to quantify stirring in diffusionless systems (e.g. Ottino 1982; Khakhar & Ottino 1986; Franjione & Ottino 1987; Ottino 1989, 1990; Muzzio, Swanson & Ottino 1991; Chakravarthy & Ottino 1996 and references therein). The mix-norm, recently introduced by Mathew *et al.* (2005), is a multiscale measure of mixing. It is defined as the root mean square of the average values of a zero-mean concentration field over a dense set of subsets contained in the flow domain. It can be used to quantify mixing in terms of the geometry of the initial concentration field in flows with or without molecular diffusion. The reader is referred to the work by Mathew *et al.* (2005) for a detailed derivation of the mix-norm and to Mathew *et al.* (2007) for an application of the mix-norm to mixing control. These two diagnostics characterize stirring in contradicting ways and present different sensitivity to the parameters considered. We discuss in detail the discrepancies between the two diagnostics.

This article is organized as follows. In § 2, we present the mathematical model used to simulate the time evolution of the vortices. In § 3, we analyse the phase portrait and the dynamics of the vortex system. In § 4, we discuss the tangle dynamics and the mechanisms responsible for the transport and stirring of fluid. In § 5, we characterize stretching and stirring in an unbounded domain. Concluding remarks are presented in § 6.

2. Mathematical modeling

The system under study is comprised of two initially elliptical, identical vortex patches embedded in an irrotational, incompressible fluid occupying a two-dimensional, unbounded domain. Each vortex is represented by a compact, simply connected area of uniform vorticity, referred to as the Kirchhoff vortex, or the vortex patch. Since viscous forces are assumed to be negligible, the vorticity transport equation guarantees the vorticity distribution inside the vortices to remain uniform and the system can be described by the Euler equations. Under these assumptions, the time evolution of the vortices can be simulated using contour dynamics. Note that the position of the joint centre of vorticity and the total angular impulse are conserved (Melander *et al.* 1986). As time evolves, however, the shape of the vortices departs from being elliptical due, in general, to self- and mutual interactions.

We adimensionalize the problem by using as a characteristic length $\sqrt{A/\pi}$ and a characteristic time $1/\omega$. Numerically, we implement contour dynamics by representing each contour C_k, $k=1$, 2, with N marker points located at coordinates $(X_{k,l}, Y_{k,l})$, $k=1, 2$ and $l=1, 2, \ldots, N$. We compute the velocity at each marker point by replacing the line integral over each contour C_k with the sum of the integrals over all circular arcs connecting adjacent marker points (see Pozrikidis 2001). We obtain

$$\boldsymbol{u}(X_{k,l}, Y_{k,l}) = -\frac{1}{4\pi}\sum_{m=1}^{2}\omega_m\sum_{n=1}^{N}\int_{E_{m,n}}\ln\left(d'^2\right)\ \boldsymbol{t}(x', y')\,\mathrm{d}l(x', y'),$$
$$k=1, 2,\ \ l=1, 2, \ldots, N, \quad (2.1)$$

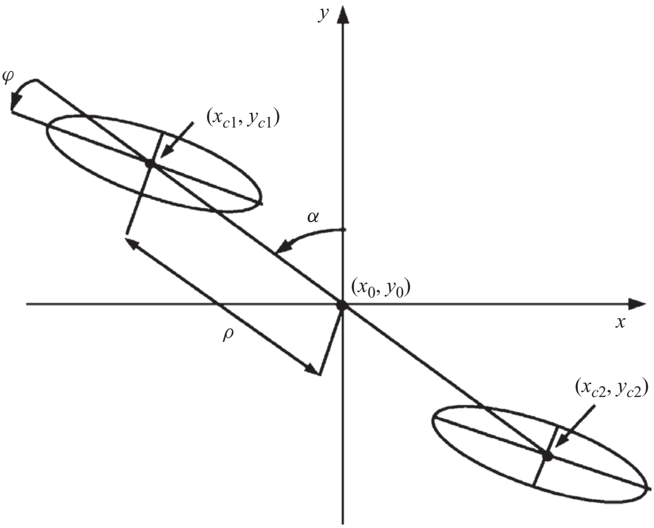

FIGURE 1. Sketch of two identical, elliptical vortex patches co-rotating symmetrically around the joint centre of vorticity (x_0, y_0) located at the origin of the Cartesian axes. The points (x_{c1}, y_{c1}) and (x_{c2}, y_{c2}) are the centroids of the patches, α is the angle of co-rotation, φ is the angle of rotation of one patch around itself and ρ is the half-separation between the centroids of the patches.

where ω_m is the vorticity of the mth patch, (x', y') are the integration variables, $d'^2 = (X_{k,l} - x')^2 + (Y_{k,l} - y')^2$ is the distance between the marker and the integration points, $E_{m,n}$ is the circular arc connecting the nth and $(n+1)$th points on the mth contour, $\boldsymbol{t}$ is the unit vector oriented counterclockwise tangent to the contour and $\mathrm{d}l$ is the differential arclength along each arc $E_{m,n}$. The motion of the contours is then obtained by integrating in time the set of $2N$ ordinary differential equations of the form

$$\frac{\mathrm{d}\boldsymbol{r}_{k,l}}{\mathrm{d}t} = \boldsymbol{u}(X_{k,l}, Y_{k,l}), \quad k = 1, 2, \quad l = 1, 2, \ldots, N, \tag{2.2}$$

where $\boldsymbol{r}_{k,l}$ is the vector identifying the lth marker point on the kth contour, i.e. $\boldsymbol{r}_{k,l} = X_{k,l}\hat{\boldsymbol{\imath}} + Y_{k,l}\hat{\boldsymbol{\jmath}}$, where $\hat{\boldsymbol{\imath}}$ and $\hat{\boldsymbol{\jmath}}$ are the axis unit vectors. The elliptical shape, position and orientation approximating the vortex patches are described by the approximate aspect ratio $\lambda = b/a$ and area A, where b and a are the approximate semi-minor and semi-major axes of the patch, respectively, the approximate coordinates of the centroids (x_{ck}, y_{ck}), $k = 1, 2$, the orientation angle φ and the co-rotation angle α. A sketch of the vortex system is shown in figure 1. Without loss of generality, in all our simulations, we consider a pair of initially elliptical vortices of area $A = \pi$ and vorticity $\omega = 1$. According to Melander *et al.* (1988), the total dimensionless angular impulse σ of the system can be written as $\sigma = 4\rho^2 + \lambda + 1/\lambda$. The latter equation is used to set the initial separation of the vortices for a chosen value of their initial angular impulse and aspect ratio, and to monitor the accuracy of the simulation by verifying the conservation of the angular impulse.

During the time evolution of the system, we recover the approximate elliptic shape, position and orientation of the vortex patches from the sequence of marker points describing each contour C_k, $k = 1, 2$. We approximate the coordinates of the centroid of a patch with the centre of mass of the marker points tracing its contour. The dimensionless centroid half-separation, ρ, is computed as the distance from the position of one of the centroids, (x_{ck}, y_{ck}), to the joint centre of vorticity (x_0, y_0). The semi-major axis, a, of the ellipse approximating the shape of the patch is obtained by computing the maximum distance between all possible pairs of marker points of the contour C and diving by 2. The semi-minor axis, b, is then computed by recalling that the area of the vortex is constant and given by $A = ab\pi = \pi$. The co-rotation angle, α, is obtained by computing the rotation of the vector identifying the centroid of a vortex with respect to its initial orientation. The rotation angle of a vortex about itself, φ, is obtained by computing the rotation of the major axis of the elliptic patch with respect to its initial orientation and then subtracting the co-rotation angle, α. Note that in all simulations presented in this article, with the exception of two cases (see figures 23*a* and 23*b*), the shape of the vortices departs from being elliptical but an ellipse can still be fitted accurately to the marker points describing the contour.

We simplify the problem and reduce the computational cost by a factor 2 by imposing radial symmetry, i.e. $\boldsymbol{r}_{1,l} = -\boldsymbol{r}_{2,l}$, $l = 1, 2, \ldots, N$. We verified that computations with and without radial symmetry imposed are identical. Consequently, we drop the subscript k identifying the two vortex patches. We choose the initial number of marker points, N, as the smallest integer such that $L_c/N < 0.05$, where L_c is the initial length of the contour C of the vortex patch. The spatial accuracy is preserved during the simulation by introducing a new marker point when the distance between two adjacent marker points becomes larger than 0.1 or, in the case of high curvature, when the angle subtended by the circular arc becomes greater than $\pi/4$. The time integration is performed using a second-order Runge–Kutta scheme with time step $\mathrm{d}t = 0.05$.

3. Phase portrait and system dynamics

In this section, we discuss the phase portrait and the time evolution of the variables describing the approximate elliptic shape of the pair of vortices. Figure 2 shows the phase portrait in the (φ, λ)-plane. The trajectories correspond to the time evolution of the pairs of co-rotating, initially elliptic vortices of angular impulse $\sigma = 24.4$, starting from the following initial conditions: orientation $\varphi = 0$ and aspect ratios $\lambda = 0.40, 0.50, 0.60, 0.70, 0.80, 0.84, 0.8947$. For the sake of clarity, we present the phase portrait unwrapped over the interval $-\pi < \varphi \leqslant \pi$. Note, however, that for this choice of the angular impulse, the phase portrait is not strictly periodic because the vortices depart from being elliptical due, in general, to self-interaction and mutual interaction.

The phase portrait is characterized by an elliptic point located at $(\varphi = 0, \lambda \approx 0.8947)$ and a separatrix, which divides the portrait into two regions, see figure 2. In one region, the open trajectories represent vortex patches rotating around themselves while co-rotating around the joint centre of vorticity (x_0, y_0). In the other region, the trajectories encircling the elliptic point represent vortex patches that co-rotate around the joint centre of vorticity, while their shape oscillates in time around the initial orientation $\varphi = 0$. The trajectories encircling the elliptic point are not perfectly closed curves because the vortex system is affected by noise due to the numerical discretization, small deviations of the patches from the elliptic shape and the fact that the rotation angle φ is less accurately computed as the shape of the vortex patches becomes close to circular. The elliptic point $\lambda = 0.8947$ is the limiting case of the latter type of motion and identifies a pair of nearly circular patches whose rotation angle, φ, is nearly zero. In figure 2, this point appears as a dot because the aspect ratio of the patches is affected by perturbations of order $\mathcal{O}(10^{-4})$. The dynamics of pairs of

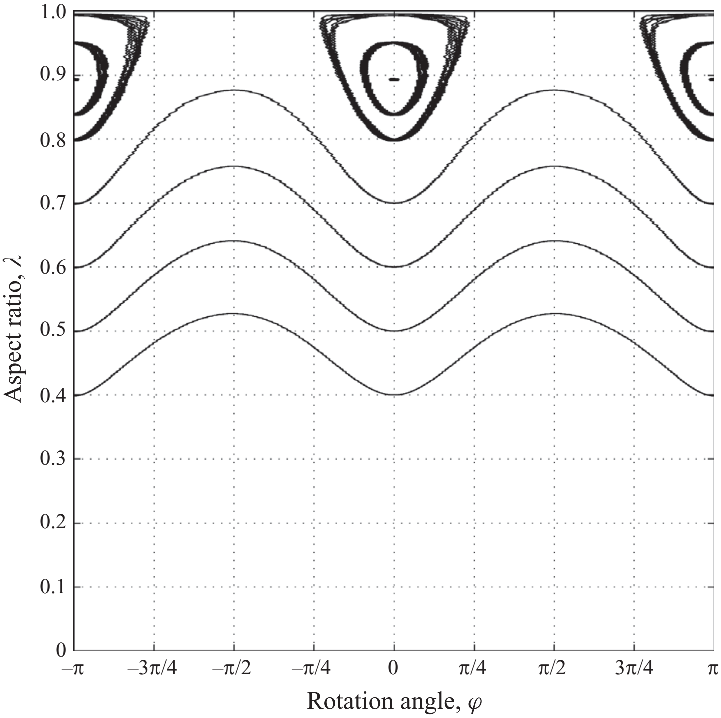

FIGURE 2. Phase portrait of a pair of co-rotating initially elliptic vortices of angular impulse $\sigma = 24.4$ with the following initial conditions: $\varphi = 0$ and $\lambda = 0.40, 0.50, 0.60, 0.70, 0.80, 0.84, 0.8947$.

vortices with an initial aspect ratio less than 0.40 is not represented because, for the angular impulse $\sigma = 24.4$, the vortex patches rapidly lose their elliptic shape and start merging within half a period of co-rotation (cf. Melander *et al.* 1988; Cerretelli & Williamson 2003*a*).

In figure 3(*a*), we compare the time evolution of the co-rotation angle, α, for pairs of elliptic vortices of initial aspect ratios $\lambda = 0.40$ and 0.8947. The co-rotation angle oscillates mildly with time, following a linear trend, and the slope indicates that the angular velocity of co-rotation increases as the initial aspect ratio decreases. Indeed, the first period of co-rotation is about 134.50 for $\lambda = 0.40$ and 139.90 for the limiting case $\lambda = 0.8947$.

Figure 3(*b*) shows the time evolution of the rotation angle, φ, for pairs of vortices of initial aspect ratios $\lambda = 0.40, 0.50, 0.60, 0.70, 0.84, 0.8947$. The results are in accordance with the phase portrait, see figure 2. The behaviour of the rotation angle changes radically for open and closed trajectories. For open trajectories, i.e. $0.40 \leqslant \lambda < 0.80$, the average angular velocity increases as the initial aspect ratio increases. Also, the amplitude and frequency of the fluctuation of the rotation angle increase for increasing values of the initial aspect ratio. For closed trajectories, i.e. $0.80 \leqslant \lambda \leqslant 0.8947$, the average angular velocity is zero, because the shape of the vortices oscillates with respect to the initial orientation of the patches. The amplitude of the oscillations decreases while the frequency increases with the aspect ratio. Hence, the separatrix in the phase portrait identifies a jump in the dynamics of the vortex pair.

Figure 3(*c*) shows the time evolution of the half-separation of the centroids, ρ, for pairs of vortices with initial aspect ratios $\lambda = 0.40$, 0.60, 0.84, 0.8947. Due to

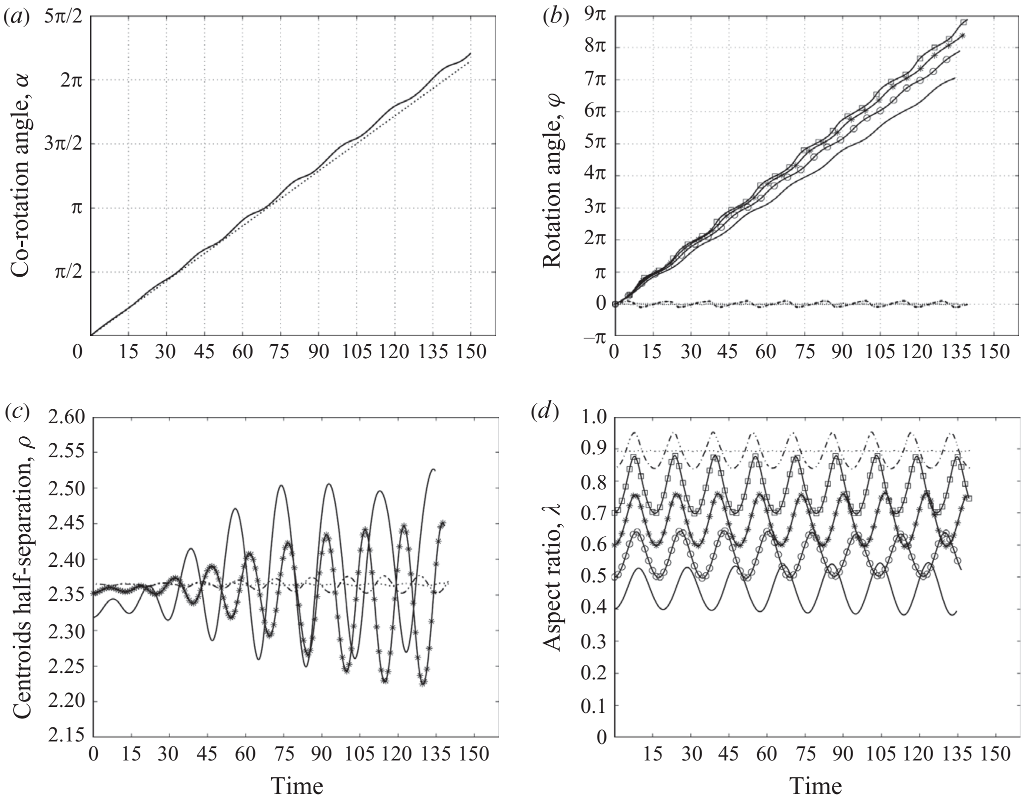

FIGURE 3. (*a*) Time evolution of the co-rotation angle α. (*b*), (*c*) and (*d*) Time evolution, over one period of co-rotation, of the rotation angle φ, the half-separation of the centroids ρ and the aspect ratio λ, respectively. Vortex pairs are identified by their initial aspect ratios $\lambda = 0.40$ (solid line), 0.50 (○), 0.60 (∗), 0.70 (□), 0.84 (dash-dotted) and 0.8947 (dotted).

a strong mutual interaction and a gradual departure from the elliptic shape, the initial half-separation of two vortex patches oscillates with time. The amplitude of the fluctuations increases for decreasing values of the aspect ratio, while the frequency increases for increasing values of the aspect ratio.

Figure 3(*d*) shows the time evolution of the aspect ratio, λ, for pairs of vortices of initial aspect ratios $\lambda = 0.40$, 0.50, 0.60, 0.70, 0.84, 0.8947. The amplitude of the oscillations increases as the initial aspect ratio increases from $\lambda = 0.40$ up to $\lambda \approx 0.80$. The trend abruptly reverses as the separatrix is crossed, providing further evidence that there exists a jump in the dynamics of the vortex pair. The amplitude decreases for $\lambda > 0.80$ and becomes nearly zero for the limiting case $\lambda \approx 0.8947$.

4. Tangle dynamics and fluid transport

The geometry of the flow induced by a pair of like-signed elliptic vortices, when seen in a frame of reference rotating with the vortex pair, can be deduced plotting the level set of the associated stream function $\psi_r(t, x, y)$ (Dritschel 1985; Melander *et al.* 1988; Fuentes 2001; Cerretelli & Williamson 2003*a*,*b*), which is given by the transformation (Fuentes 2001)

$$\psi_r(t, x, y) = \psi_f(t, x, y) + \tfrac{1}{2}\ \Omega(t)\ [(x - x_0)^2 + (y - y_0)^2], \tag{4.1}$$

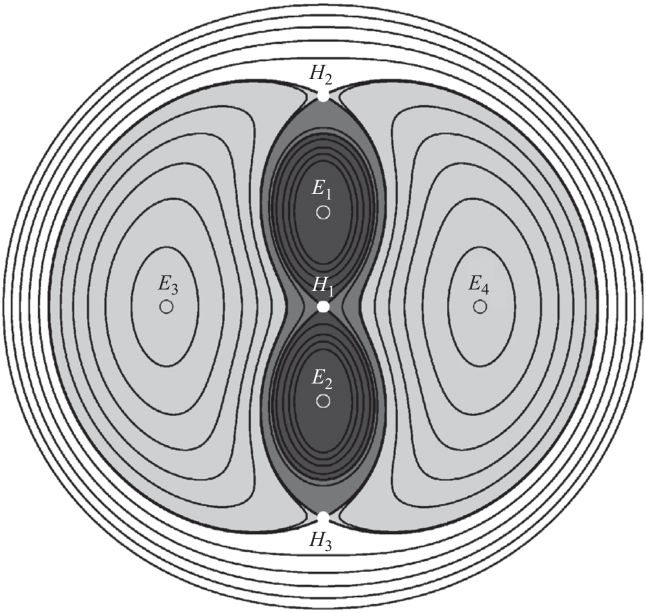

FIGURE 4. Stream function at time $t = 0$ as observed in a rotating frame of reference. The elliptic points E_1 and E_2 are due to the presence of the real vortices, while E_3 and E_4, called 'ghost vortices', are due to the rotating frame. The hyperbolic points are labelled H_1, H_2 and H_3, and their homoclinic and heteroclinic orbits define the inner core regions (black), the inner recirculation region (dark grey), the outer recirculation regions (light grey) and the outer flow (white).

where $\psi_f(t, x, y)$ is the stream function at time t as observed in a fixed frame of reference, $\Omega(t)$ is the angular velocity of the rotating frame of reference chosen equal to the co-rotation angular velocity of the vortex pair and (x_0, y_0) are the coordinates of the centre of co-rotation of the patches, i.e. the joint centre of vorticity. Figure 4 shows, at time $t = 0$, the stream function ψ_r. The three hyperbolic and four elliptic points are shown as filled and open circles, respectively. The elliptic points, E_1 and E_2, are due to the presence of the vortices and coincide with their centroids, while the other two, E_3 and E_4, called 'ghost vortices' (Melander *et al.* 1988), appear as a consequence of using a rotating frame. The hyperbolic points labelled H_1, H_2 and H_3 are connected by heteroclinic or homoclinic orbits. These orbits, also called 'separatrices', divide the flow into different regions (Cerretelli & Williamson 2003*a*): the *outer* (or free-flow) region, where fluid particles simply move around the vortex system; two outer recirculation regions, where particles rotate around the 'ghost' vortices; an inner recirculation region, where particles rotate around the two real vortices and two inner core regions, one for each real vortex, that have in common solely the hyperbolic point H_1. In figure 4, these regions are depicted with different shades of grey. Note that the size and shape of these regions depend on the initial aspect ratio of the vortices, but the topology of the fixed points and the separatrices is common to all cases.

We consider as the unperturbed system the velocity field and streamlines associated with the initial condition when the major axes of the vortex patches are aligned. During the time evolution, the rotation of the patches on themselves generates a time-periodic perturbation of the velocity field as the aspect ratio λ, separation of the centroids 2ρ and rotation angle φ of the patches change with time, see figures 3(*b*) to 3(*d*). This perturbation has a strong effect on the geometry of the heteroclinic and homoclinic orbits. If the perturbation is sufficiently strong, the separatrices of the unperturbed flow, represented in figure 4, form complicated structures, called *chaotic tangle*. The orbits still depart smoothly from the corresponding hyperbolic point, but undergo to strong oscillations as they approach a different hyperbolic point, for heteroclinic orbits, or the same point, for homoclinic orbits. The analysis of the tangle dynamics (e.g. Rom-Kedar *et al.* 1990) is fundamental for understanding fluid transport in time-periodic flows. Rom-Kedar *et al.* (1990) performed a dynamical system type of analysis of a two-dimensional, inviscid, incompressible flow comprised of a pair of point vortices of opposite sign and an oscillating strain field. In the absence of perturbations, i.e. the strain field, the vortex pair translates with constant velocity and transports a constant amount of fluid trapped in the recirculation zones. On the contrary, when the strain field is added, fluid is entrained and detrained from the recirculation zones and chaotic particle motion occurs. Rom-Kedar *et al.* (1990) have shown that the transport and dispersion of fluid particles can be quantified by analysing the intersections of the stable and unstable manifolds at given time slices. In this study, given the finite time and aperiodicity of the vortex system, we use tangle dynamics to describe the transport of fluid induced by a vortex pair over a finite time, namely one period of co-rotation.

To characterize the perturbations affecting the homoclinic orbit stemming from the hyperbolic point H_1, we perform a linear stability analysis of the velocity field induced by a pair of elliptic vortices about the joint centre of vorticity. Expanding in Taylor series the two components of the velocity field (D. Vainchtein 2005, private communication), we obtain

$$\begin{aligned} U(x,y) &= M_{11}x + M_{12}y \\ &= C_1\,[\kappa_1 y + 2\kappa_2 x] \\ &\quad + C_2\{\cos(2\psi)[\kappa_3 y + 4\kappa_1\kappa_2 x] + \sin(2\psi)[\kappa_3 x - 4\kappa_1\kappa_2 y]\}, \end{aligned} \tag{4.2}$$

$$\begin{aligned} V(x,y) &= M_{21}x + M_{22}y \\ &= C_1\,[\kappa_1 x - 2\kappa_2 y] \\ &\quad + C_2\{\cos(2\psi)[\kappa_3 x - 4\kappa_1\kappa_2 y] - \sin(2\psi)[\kappa_3 y + 4\kappa_1\kappa_2 x]\}, \end{aligned} \tag{4.3}$$

where

$$C_1 = \frac{1}{\rho^4}, \quad C_2 = \frac{3}{4\rho^8}\frac{1-\lambda^2}{\lambda}, \tag{4.4}$$

$$\kappa_1 = y_c^2 - x_c^2, \quad \kappa_2 = x_c y_c, \quad \kappa_3 = x_c^4 - 6x_c^2 y_c^2 + y_c^4, \tag{4.5}$$

and (x_c, y_c) are the coordinates of the centroid of one patch, with the other located at $(-x_c, -y_c)$. The eigenvalues and eigenvectors of the matrix $\boldsymbol{M}$ determine the dynamics of the flow in the neighbourhood of the hyperbolic point (x_0, y_0). The two eigenvalues are real, equal in magnitude and opposite in sign for any value of the aspect ratio. Thus, the point H_1 is a saddle point during the entire evolution of the system. The two eigenvectors represent two subspaces: the unstable subspace, identified by the eigenvector corresponding to the real positive eigenvalue, and the stable subspace, identified by the eigenvector corresponding to the real negative eigenvalue. These spaces are invariant subspaces of the linearized equations. As for the linearized

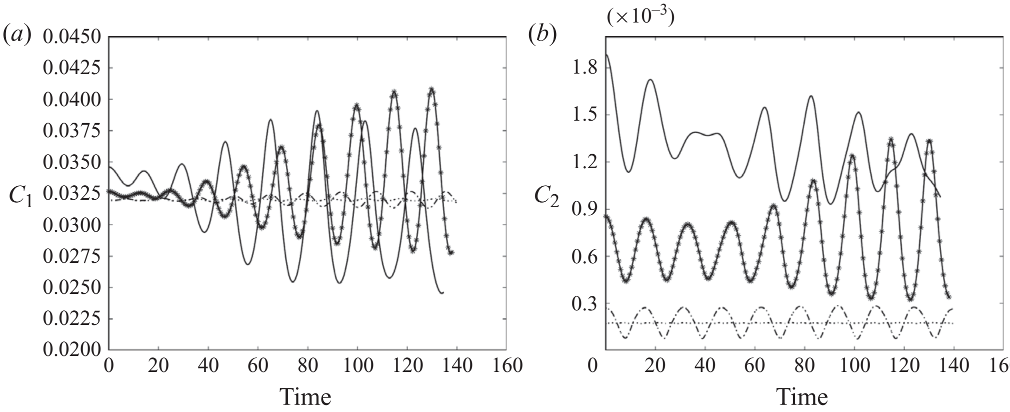

FIGURE 5. Time evolution of the coefficients C_1 (a) and C_2 (b) of the strain field induced around the hyperbolic point located at the joint centre of vorticity (x_0, y_0) by pairs of elliptic vortices of initial aspect ratios $\lambda = 0.40$ (solid line), $\lambda = 0.60$ (∗), 0.84 (dash-dotted) and 0.8947 (dotted).

system, the nonlinear system has two invariant manifolds: the stable manifold, which consists of the orbits of the nonlinear system tangent to the stable subspace, and similarly an unstable manifold which is tangent to the unstable subspace.

Hence, (4.2) and (4.3) describe a strain field generated by the vortex pair around the point (x_0, y_0). The first term on the right-hand side depends solely on the coordinates of the centroids and is responsible for the time modulation of the amplitude of the strain field. The second term, instead, depends on the coordinates of the centroids, the aspect ratio, λ, and the angle $\psi = \alpha + \varphi$, which is the sum of the co-rotation, α, and rotation, φ, angles, and is responsible for the angular reorientation of the strain field. Figures 5(a) and 5(b) show the time evolution of the coefficients C_1 and C_2, respectively, for pairs of elliptic vortices of initial aspect ratios $\lambda = 0.40$, 0.60, 0.84 and 0.8947. Note that the average value of the coefficient C_2 is nearly two orders of magnitude smaller than C_1 and, also, that the value of both coefficients oscillates in time with amplitude increasing and frequency decreasing as the aspect ratio decreases. Figure 6 shows, over a period of co-rotation, the angles swept by the eigenvectors of the stability matrix $\boldsymbol{M}$. The eigenvectors for the case $\lambda = 0.40$ oscillate nearly 12°, see figure 6(a). This oscillation reduces to nearly 1° for the case $\lambda = 0.84$, see figure 6(b).

Under the action of the strain field (4.2)–(4.3), the stable and unstable manifolds of the hyperbolic points deform and create a tangle. Following the work by Fuentes (2001, 2005), we compute, in correspondence to the time slice $t_0 = 0$, the tangle formed by the orbits of the saddle point H_1. The unstable manifold is obtained by selecting, at time $t_0 - \Delta t$, a short material line of length $l = 0.04$ crossing, along the direction of the unstable eigenvector, the saddle point H_1 and evolving it up to $t = t_0$ in the rotating frame of reference. Similarly, the stable manifold at time t_0 is obtained by selecting, at time $t_0 + \Delta t$, a short material line of length $l = 0.04$ crossing, along the direction of the stable eigenvector, the saddle point H_1 and evolving it backwards in time up to $t = t_0$ in the rotating frame of reference. The time interval Δt is chosen sufficiently large to allow a clear and quite complete development of the manifolds. Figure 7 shows the intersections of the stable and unstable manifolds with the time slice $t_0 = 0$, computed using a time interval Δt corresponding to three periods of rotation, $3T$, of

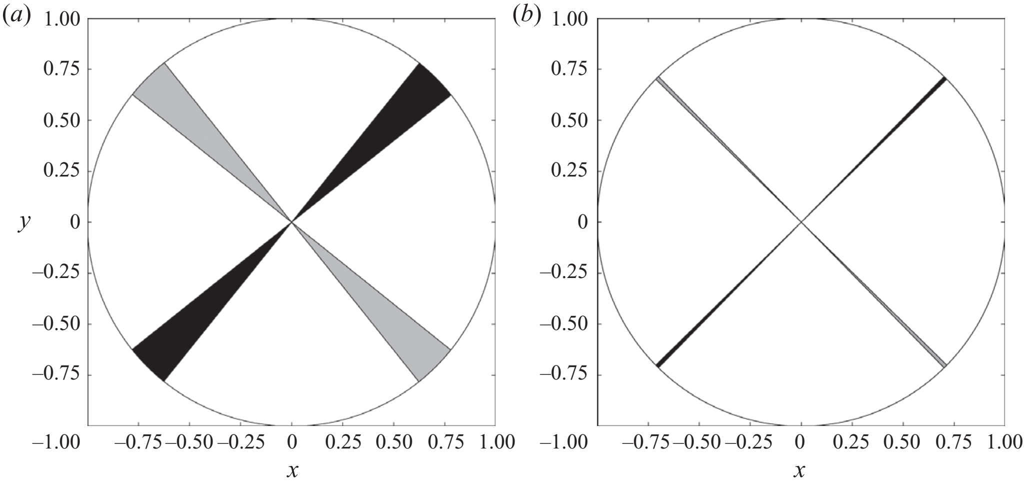

FIGURE 6. Angular range swept, over a period of co-rotation, by the eigendirection of the unstable (black) and stable (grey) manifolds computed for pairs of elliptic vortices of initial aspect ratios $\lambda = 0.40$ (*a*) and 0.84 (*b*).

the elliptic vortices with initial aspect ratios $\lambda = 0.40$, 0.60, and three and six periods of oscillation of the vortices with aspect ratio $\lambda = 0.80$. The different motion of the vortices with aspect ratio $\lambda < 0.80$ or $\lambda \geqslant 0.80$ has major effects on the structure of the tangle formed by the separatrices. When $\lambda < 0.80$, large perturbations are created by the rotation of the patches, and few periods of rotation are sufficient for the tangle to develop and show its complexity. In this range of λ, the vortices perform complete rotations around themselves and wind the separatrices in a tight spool around their contours. The complexity of the tangle increases as the initial aspect ratio decreases, see figure 7(*a*–*b*). On the contrary, when $\lambda \geqslant 0.80$, the shape of the vortices oscillates around its initial orientation yielding a weaker perturbation and, therefore, the loss of the wrapping mechanism. The separatrices, being only slightly deformed, overall maintain their unperturbed structure. Figures 7(*c*) and 7(*d*) show, as an example, the tangle for $\lambda = 0.80$. In this case, the deformations of the tangle are minimal when Δt corresponds to three periods of oscillation and slightly increase when computed over six periods of oscillation.

To investigate the transport of fluid generated by a pair of co-rotating initially elliptic vortex patches of initial aspect ratio $\lambda = 0.40$, we simulate the time evolution of three material lines coinciding, at $t = 0$, with the separatrices of the co-rotating stream function, depicted in figure 4. In other words, we simulate and analyse the tangle dynamics. We colour-code black, the fluid enclosed in the inner core regions; dark-grey, the fluid in the inner recirculation region; light-grey, the fluid in the outer recirculation regions; and white, the fluid in the outer flow. Figure 8(*a*) presents the initial distribution of the colour-coded fluid. Figure 8(*b*–*f*) shows the snapshots of the time evolution of the colour-coded fluid at times corresponding to rotation angles $\varphi = \pi/2, \pi, 3\pi/2, 2\pi$ and 4π. The evolution is characterized by large deformations of the separatrices and the formation of lobes. New lobes form and develop over every half a period of rotation, $T/2$. Note how the black and dark-grey fluids, initially enclosed in the inner core regions and in the inner recirculation region, respectively, are transported into the outer recirculation regions by complex lobes. The light-grey

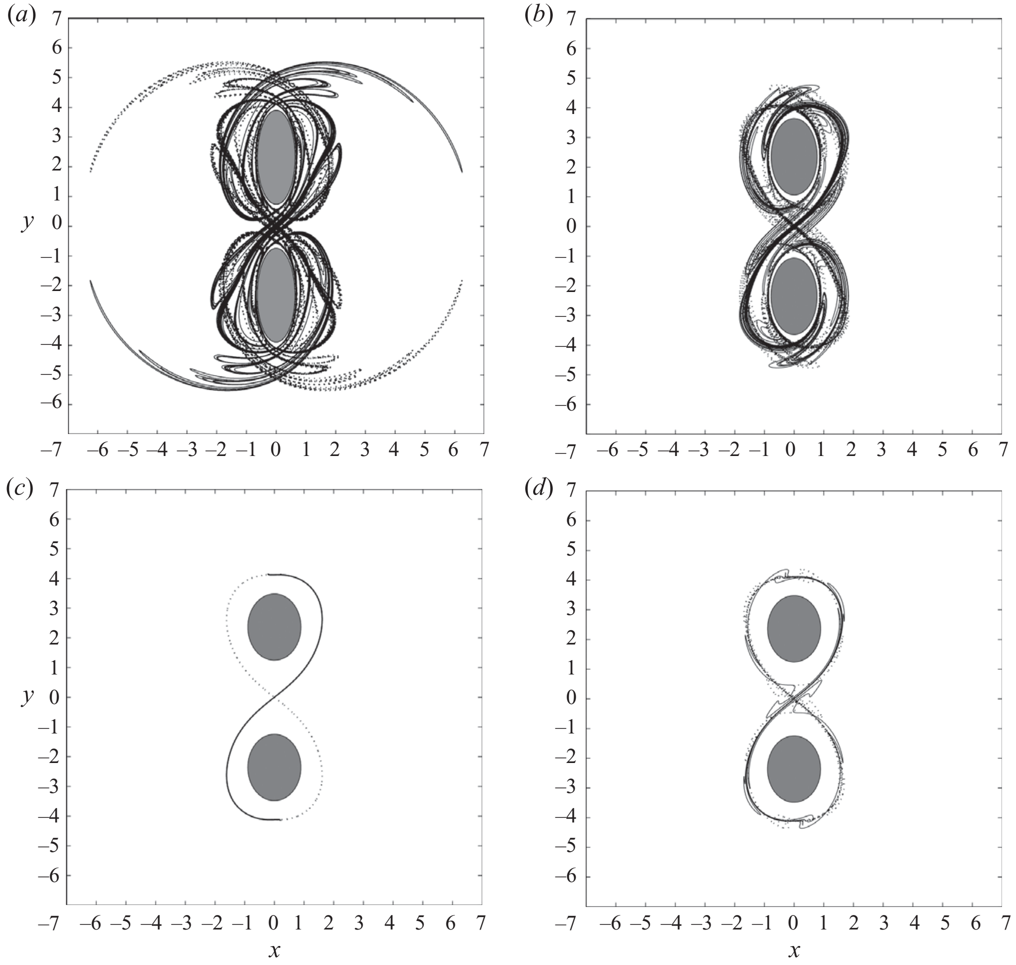

FIGURE 7. Intersections with the time slice $t_0 = 0$ of the stable (dotted line) and unstable (solid line) manifolds of the saddle point located at the joint centre of vorticity. The first row shows the results computed over three periods of rotation, $3T$, for pairs of vortices of initial aspect ratios $\lambda = 0.40$ (*a*) and 0.60 (*b*). The second row shows the results computed over three (*c*) and six (*d*) periods of oscillations for a vortex pair of initial aspect ratio $\lambda = 0.80$.

fluid, instead, tends to be entrained into the inner recirculation region surrounding the vortex patches.

Figure 9 presents a comparison of the degree of transport of the colour-coded fluid for vortex pairs of initial aspect ratios $\lambda = 0.40$ and 0.84. Note that the vortex pairs evolve differently and, consequently, the snapshot for the case $\lambda = 0.40$ is taken at a time corresponding to three periods of rotation, $3T$, while for the case $\lambda = 0.84$ the time corresponds to three periods of oscillations. As suggested by the linear stability analysis previously described, the perturbation induced around the saddle point H_1 and the deformation of its separatrices increase for decreasing values of the initial aspect ratio of the vortices. Therefore, the best transport of fluid is induced by a pair of vortices of small initial aspect ratio; in our case $\lambda = 0.40$. On the contrary, the transport of fluid is minimal for the case $\lambda = 0.84$, see figure 9(*b*).

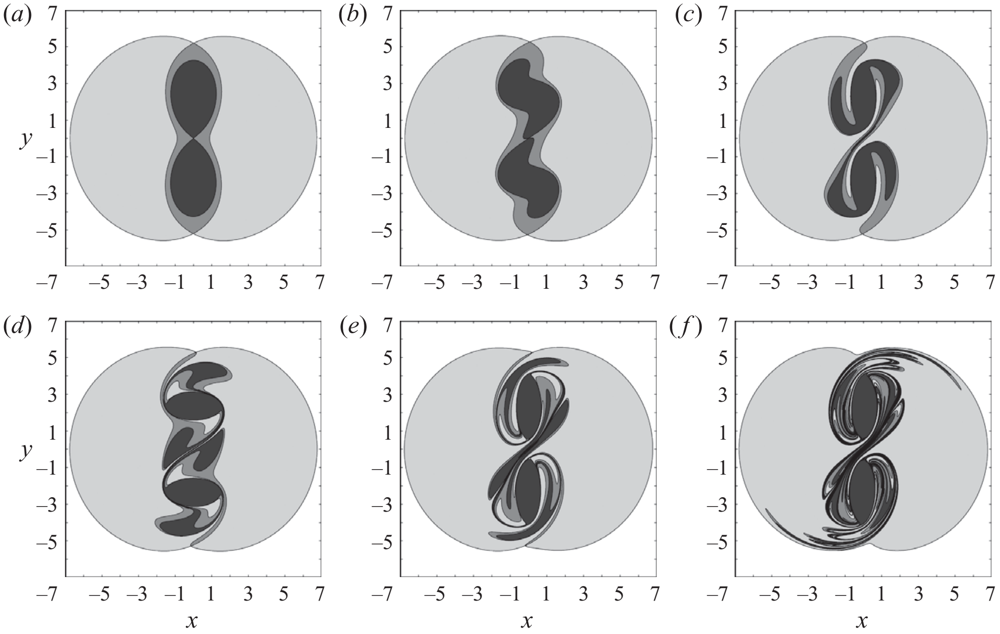

FIGURE 8. (*a*) Distribution at $t=0$ of the colour-coded fluid in the four different regions delimited by the separatrices of the co-rotating stream function, for a pair of vortices of initial aspect ratio $\lambda=0.40$: inner core regions (black), inner recirculation region (dark-grey), outer recirculation regions (light-grey) and outer flow region (white). (*b*)–(*f*) Snapshots of the time evolution of the colour-coded fluid, taken at times corresponding to rotation angles $\varphi=\pi/2$ (*b*), π (*c*), $3\pi/2$ (*d*), 2π (*e*) and 4π (*f*).

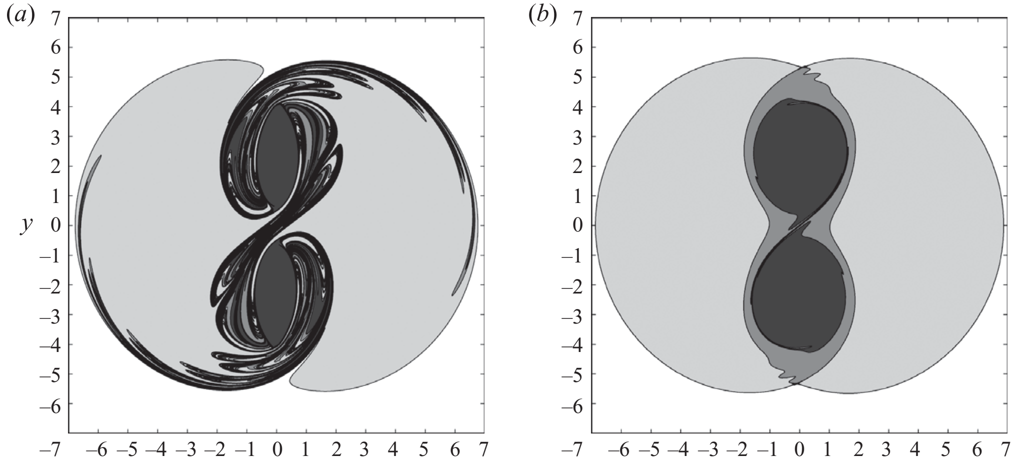

FIGURE 9. Snapshots of the transport of the colour-coded fluid after three periods of rotation for the case $\lambda=0.40$ (*a*) and three periods of oscillations for $\lambda=0.84$ (*b*).

5. Characterization of stretching and stirring

We characterize stretching and stirring on a circular domain centred at the joint centre of vorticity, (x_0, y_0), because the evolution of a pair of like-signed initially elliptic vortices has radial symmetry. The radius of the domain should be carefully chosen since the physical domain is unbounded and, consequently, the quantification of stretching and stirring depends on the radius chosen. To investigate the effect of the size of the domain, we consider three circular domains of dimensionless radii $R = 0.5$, 7 and 20. The domain of radius $R = 7$ is suggested by the dynamical system analysis presented in § 4, where it has been shown that stirring and transport are confined by the outer separatrices in a region of nearly radius 7. The domain of radius $R = 0.5$ identifies a region between the vortex pair where we expect stirring to be mostly dominated by the dynamics of the saddle point H_1 located at the joint centre of vorticity. This radius should be considered small with respect to vortex half-separation, ρ. Note that this case is characterized by a substantial transport of fluid in and out of the domain. The domain of radius $R = 20$ identifies a region where the details of the vortex interaction become negligible and stirring is dominated by the dynamics of the outer flow. This radius should be considered large with respect to the vortex half-separation, ρ. In this case, there is no transport of fluid in and out of the domain.

To investigate stretching and stirring, we consider as initial concentration of the scalar field a simple configuration often analysed in the literature, where two uniform concentrations are separated by a straight-line interface. Since stirring and stretching depend on the geometry of the initial concentration field, we explore their dependence by considering the following straight-line interfaces: $y = 0$, $y = x$, $x = 0$, $y = -x$. Recall that $y = x$ and $y = -x$ are, respectively, the eigendirections at time $t = 0$ of the unstable and stable manifolds of the hyperbolic point H_1, see § 4. Since we consider a diffusionless system, we quantify stretching simply by simulating the time evolution of the interface. However, the concentration field must be reconstructed at each time t to quantify stirring.

5.1. *Stretching*

Ottino (1989) showed that '. . .from a kinematical viewpoint fluid mixing is the efficient stretching and folding of material lines and surfaces.'. In particular, stirring leads to a typical lamellar structure. When molecular diffusion is negligible, the lamellae are separated by an interface which is passively advected, therefore maintaining its identity. As the degree of stretching of the interface increases, the contact area between the fluids increases accordingly and, consequently, the scale of segregation decreases. In this case, stirring can be quantified in terms of the number and thickness of the lamellae or in terms of stretching of the interface. When the rate of stretching of fluid elements is linear, stirring results to be minimal. On the contrary, exponential stretching can be seen as the fingerprint of chaotic motion of fluid particles and, therefore, is associated with efficient stirring. The quality of stirring, however, cannot be uniquely related to stretching but must also be evaluated in terms of the efficient distribution of stretching on the domain (Muzzio *et al.* 1991).

On a circular domain of radius $R = 0.5$, the dynamics is mostly dominated by the saddle point H_1 located at the joint centre of vorticity and the transport of fluid in and out of domain is substantial. Consequently, stretching of the interface is not well defined because segments of the interface are continuously advected in and out of the domain. In this case, therefore, we quantify stirring in terms of the number of lamellae. Figure 10(*a*–*b*) shows the linear–log plots of the time evolution of the number of lamellae produced by pairs of vortices of initial aspect ratios $\lambda = 0.40$ and 0.84, when the initial interfaces are $y = 0$, $y = x$, $x = 0$ and $y = -x$. Note that the number of lamellae is a discontinuous function of time; however, for convenience, we plot it as a continuous function. For a given initial orientation of the interface,

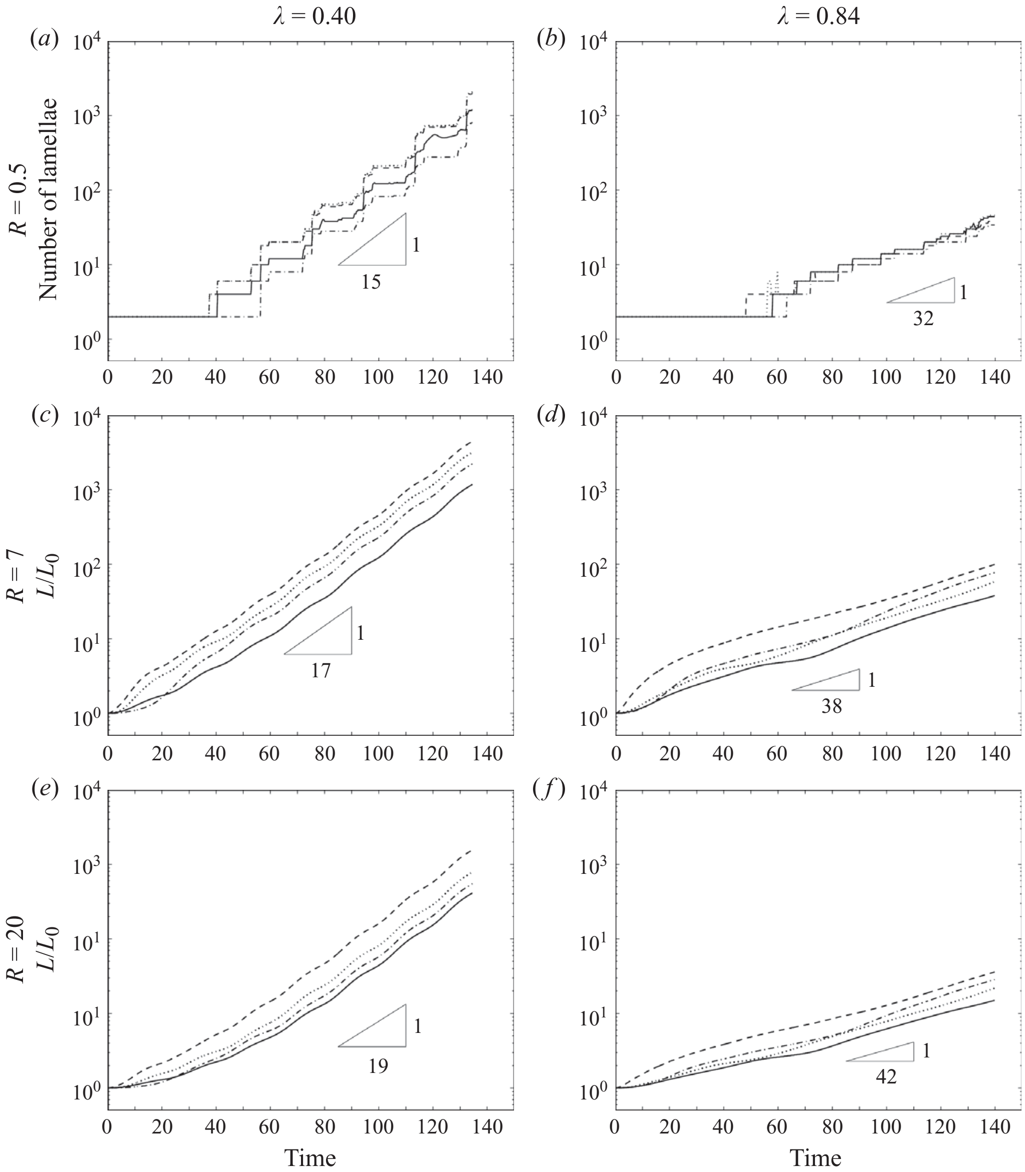

FIGURE 10. (*a*)–(*b*) Linear–log plots of the time evolution of the number of lamellae computed on a domain of radius $R = 0.5$, for pairs of co-rotating vortices of initial aspect ratios $\lambda = 0.40$ (*a*) and 0.84 (*b*). (*c*)–(*f*) Linear–log plots of the stretching of the interface induced by pairs of co-rotating vortices of initial aspect ratios $\lambda = 0.40$ and 0.84, computed on circular domains of radii $R = 7$ and 20. The initial orientations of the interface are: $y = 0$ (solid line), $y = x$ (dotted), $x = 0$ (dashed) and $y = -x$ (dash-dotted).

the time evolution of the number of lamellae is exponential and increases as the initial aspect ratio decreases. Initially, no lamellae are formed. As the number of lamellae starts increasing, the growth rate depends on the initial aspect ratio of the vortices. For $\lambda = 0.40$, the number of lamellae increases in well-distinct steps, each step separated from the next by nearly half a period of rotation. This behaviour is lost for the case $\lambda = 0.84$, where the number of lamellae increases in small and asynchronized steps. This is due to the fact that the dynamics of the saddle point H_1 is increasingly more perturbed by the rotational motion of the vortices and stirring is more chaotic, as the initial aspect ratio of the patches decreases. The overall time evolution of the number of lamellae is exponential with time: for $\lambda = 0.40$ it scales as $\sim\exp(t/15)$, whereas for $\lambda = 0.84$ it scales as $\sim\exp(t/32)$.

On the circular domains of radii $R = 7$ and $R = 20$, since the transport of fluid in and out of the domain is negligible, we quantify stirring in terms of stretching of the interface. Figure 10(*c–f*) shows the linear–log plots of the time evolution of the ratio $L(t)/L_0$, where $L(t)$ is the length of the interface at time t and $L_0 = R$ is the length at time $t = 0$, induced by pairs of vortices of initial aspect ratio $\lambda = 0.40$ (*c* and *e*) and $\lambda = 0.84$ (*d* and *f*), for the four initial interfaces considered. Stretching increases as the initial aspect ratio decreases in all cases. In particular, the time evolution of stretching is exponential in time for all the aspect ratios considered and, therefore, can be expressed as

$$\frac{L(t)}{L_0} \propto \mathrm{e}^{(\beta t)}, \tag{5.1}$$

where β is a coefficient dependent, as we will discuss later, on the rate of divergence of nearby trajectories.

On the domain $R = 7$, which encloses the outer recirculation regions shown in figure 4, stretching is dominated by the rotational and co-rotational motion of the vortices, and it is sensitive to both initial aspect ratio of the vortices and initial geometry of the concentration field. Figures 10(*c*) and 10(*d*) show that the vertical interface, $x = 0$, undergoes to the highest degree of stretching because it crosses, at $t = 0$, the two vortices and passes through the two elliptic points, E_1 and E_2, located at their centroids. Hence, during the evolution, the interface is wrapped into a tight spiral around the vortices due to their rotational motion. On the contrary, the interface $y = 0$ undergoes to the lowest degree of stretching because it crosses at $t = 0$ the elliptic points E_3 and E_4 of the two 'ghost' vortices where the motion is laminar and recirculation is slow. The degree of stretching for $\lambda = 0.40$ is characterized by $\beta \approx 1/17$, while for $\lambda = 0.84$ we have $\beta \approx 1/38$. This substantial difference can be explained by recalling that the vortices of initial aspect ratio $\lambda < 0.80$ undergo to complete rotations around their initial orientation inducing, therefore, a tight wrapping of the interface. On the contrary, the shape of vortices with $\lambda \geqslant 0.80$ undergoes to oscillations around the initial orientation and, consequently, the wrapping of the interface is substantially reduced. Figures 10(*e*) and 10(*f*) show that the time evolution of stretching computed on a domain of radius $R = 20$ is similar to the case $R = 7$. The interfaces $x = 0$ and $y = 0$ still undergo to the highest and lowest degree of stretching, respectively, and the order of magnitude of the degree of stretching is nearly equivalent. The reason is that the fluid contained in the free-flow region, i.e. $R > 7$ (figure 4), undergoes to laminar transport around the vortex system and, consequently, the degree of stretching of the segment of the interface that is contained in the free-flow region is negligible compared to the stretching induced within the region of radius $R = 7$. In the case $R = 20$, the values of β for the aspect ratios $\lambda = 0.40$ and 0.84 are slightly lower than in the case $R = 7$, because the initial length of the interface is nearly three times longer than in the case $R = 7$. This indicates that stretching is not sensitive to the size of the domain, provided the domain contains the separatrices.

Figure 10(*a*) shows that for the case $\lambda = 0.40$, on the domain $R = 0.5$, the time evolution of the number of lamellae is clearly synchronized with the half-period of rotation of the vortices. Unexpectedly, this relationship seems to be lost, beside a

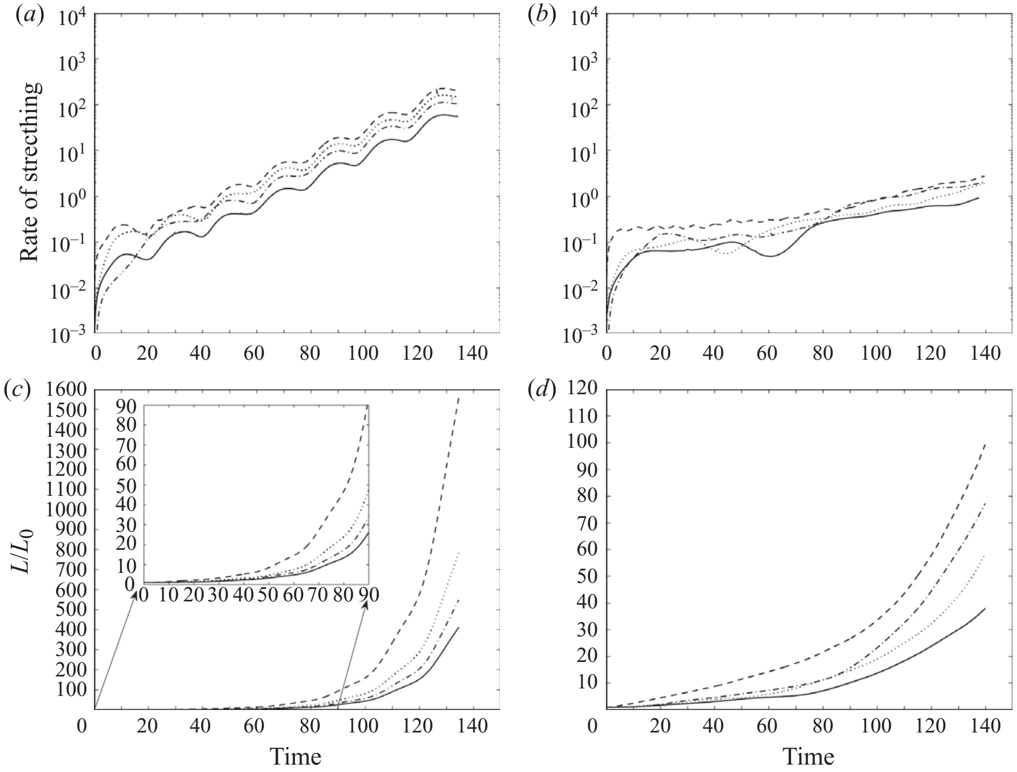

FIGURE 11. (*a*)–(*b*) Linear–log plots of the time evolution of the rate of stretching induced by pairs of co-rotating vortices of initial aspect ratios $\lambda = 0.40$ (*a*) and $\lambda = 0.84$ (*b*), computed on a circular domain of radius $R = 7$. (*c*)–(*d*) Lin–lin plots of the stretching induced by pairs of co-rotating vortices of initial aspect ratios $\lambda = 0.40$ (*c*) and $\lambda = 0.84$ (*d*), on a circular domain of radius $R = 7$. The initial orientations of the interface are: $y = 0$ (solid line), $y = x$ (dotted), $x = 0$ (dashed) and $y = -x$ (dash-dotted).

weak ondulation, when we plot the time evolution of stretching for the domains $R = 7$ (figure 10*c*) and $R = 20$ (figure 10*e*). The rate of stretching, however, is more revealing. Figure 11(*a*–*b*) shows the time evolution of the rate of stretching of all four initial interfaces, computed on a domain of radius $R = 7$, for pairs of vortices of initial aspect ratios $\lambda = 0.40$ and 0.84. In the case $\lambda = 0.40$, the rate of stretching increases in steps about every half a period of rotation of the vortices, and its average value grows of about a factor 3.25 at each step. The synchronization of stretching with half a period of rotation of the vortices can clearly be seen by plotting stretching on a linear–linear plot. Figure 11(*c*) shows that the time evolution of stretching is almost linear over every half a period of rotation of the patches but overall exponential. This behaviour is lost when $\lambda = 0.84$, see figures 11(*b*) and 11(*d*). This behaviour appears to be strongly correlated with the fact that pairs of vortices describing open trajectories in the phase portrait (figure 2), i.e. with initial aspect ratio less than about 0.80, undergo complete rotations around themselves while co-rotating around the joint centre of vorticity. On the contrary, in the range $0.80 \leqslant \lambda \leqslant 0.89$, the shape of the vortices undergoes to small and fast oscillations around the initial orientation, $\varphi = 0$, while the patches co-rotate around the joint centre of vorticity. Hence, stretching induced by the coupling between rotation and co-rotation of the patches is overall

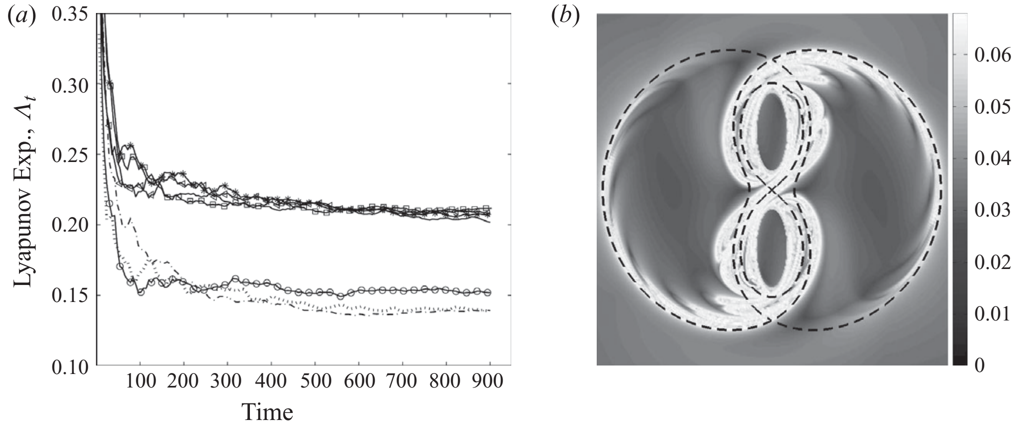

FIGURE 12. (*a*) Finite-time Lyapunov exponent, Λ_t, computed for the evolution of pairs of vortices of initial aspect ratios $\lambda = 0.40$ (solid line), 0.50 (◁), 0.60 (∗), 0.70 (□), 0.80 (○), 0.84 (dashed-dotted) and 0.8947 (dotted). (*b*) Direct expansion rate at a time corresponding to one period of co-rotation, computed for pair of vortices with initial aspect ratio $\lambda = 0.40$. The dashed lines identify the separatrices of the system, see figure 4.

exponential and increases as the initial aspect ratio of the vortex pair decreases from 0.8947 to 0.40.

To substantiate the finite-time analysis of stretching presented so far, we compute the Lyapunov exponents, which provide an estimate of the local rate of divergence of initially infinitesimally close trajectories. In practice, it suffices to calculate the maximum Lyapunov exponent, Λ_{max}, because it uniquely determines whether the system is chaotic or not. It is defined as

$$\Lambda_{max} = \lim_{t \to \infty} \frac{1}{t} \log \frac{\mathrm{d}(t)}{\mathrm{d}_0}, \tag{5.2}$$

where $\mathrm{d}(t)$ and d_0 are the distances at time t and $t = 0$, respectively, between a reference and a test orbit. Since the vortex system is a finite-time system, we resort to compute the finite-time Lyapunov exponent, Λ_t, from a set of time-series data (Wolf *et al.* 1985). To compute Λ_t, we choose a point near the saddle point, compute its trajectory for nearly seven periods of co-rotation and average the results obtained from the time series of the x and y coordinates of this test orbit. This provides us with a large set of data whose time evolution is sufficiently long for the finite-time Lyapunov exponent to converge to its asymptotic value. Note that chaotic flows present two main features: first, an exponential stretching of material lines and second, in general, different rates of stretching at different spatial locations. Therefore, exponential stretching of a material line can be characterized as in (5.1), where β is a coefficient obtained by averaging the Lyapunov exponents computed over the length of the line (Franjione & Ottino 1987).

Figure 12(*a*) shows the time evolution of the finite-time Lyapunov exponent Λ_t, computed for pairs of vortices of initial aspect ratios $\lambda = 0.40$, 0.50, 0.60, 0.70, 0.80, 0.84 and 0.8947, for a test orbit initially located at (0.1, 0.1), i.e. near the saddle point H_1, which is the region of the flow with the highest rate of stretching. Figure 12(*a*) shows that Λ_t has two well-separated asymptotic values: $\Lambda_t \approx 0.21$ for $0.40 \leqslant \lambda < 0.80$ and $\Lambda_t \approx 0.15$ for $\lambda \geqslant 0.80$. This can be explained as follows. On the one hand, vortices with $\lambda < 0.80$ perform complete rotations around themselves inducing a strong perturbation to the dynamics of the saddle point H_1. Hence, the geometry of the separatrices is radically altered and chaotic motion is induced. On the other hand, when $\lambda \geqslant 0.80$ the shape of the vortices oscillates around the initial orientation and the induced perturbation in the region of the saddle point H_1 is minimal, but not negligible. Consequently, the value of the finite-time Lyapunov exponent is comparable for pairs of vortices of initial aspect ratio $\lambda < 0.80$, but it radically decreases when the aspect ratio becomes greater than 0.80. This result provides further evidence of a jump in the dynamics of the vortex system as the initial aspect ratio becomes greater than 0.80.

To provide a qualitative overall picture of the relationship between stretching of fluid elements and their initial spatial location, we apply the set-oriented method, introduced by Padberg *et al.* (2009), to compute the direct expansion rate (Haller 2001; Padberg *et al.* 2009). The direct expansion rate measures, over a finite time, the maximum relative exponential divergence of the trajectories of two points initially separated by a small distance and, consequently, characterizes the details of the invariant manifolds of the hyperbolic points of a system, (Haller 2001; Padberg *et al.* 2009). Note that the direct expansion rate is related to the finite-time Lyapunov exponents. The direct expansion rate at time t is defined as

$$\Gamma_\varepsilon(t, \boldsymbol{x}_0) \doteq \frac{1}{t - t_0} \ln \left(\max_{\boldsymbol{x}:\|\boldsymbol{x}_0 - \boldsymbol{x}\| = \varepsilon} \frac{\| f^t(\boldsymbol{x}_0) - f^t(\boldsymbol{x}) \|}{\varepsilon} \right), \tag{5.3}$$

where ε is the initial distance between the points $\boldsymbol{x}_0$ and $\boldsymbol{x}$, $f^t(\boldsymbol{x}_0)$ is the trajectory at time t of the point $\boldsymbol{x}_0$ and $f^t(\boldsymbol{x})$ is the trajectory at time t of the point $\boldsymbol{x}$. The set-oriented method introduced by Padberg *et al.* (2009) to evaluate Γ_ε is based on two steps. First, the domain of interest is discretized with a collection of n boxes B_k, $k = 1, 2, \ldots, n$, and, second, the direct expansion rate for each box B_k is computed as

$$\Xi_\varepsilon(t, B_k) \doteq \max_{\boldsymbol{x}_0 \in B_k} \tilde{\Gamma}_\varepsilon(t, \boldsymbol{x}_0, B_k), \qquad k = 1, 2, \ldots, n, \tag{5.4}$$

where $\tilde{\Gamma}_\varepsilon(t, \boldsymbol{x}_0, B_k)$ represents the approximation of $\Gamma_\varepsilon(t, \boldsymbol{x}_0)$ computed for the box B_k. The above quantity can be obtained by filling each box with a finite number of pairs of particles and computing the maximum expansion for this set of particles. Hence, the resolution of the computation depends on the number of boxes adopted and the number of pairs of particles introduced in each box. We discretize the domain $(-7 \leqslant x \leqslant 7) \times (-7 \leqslant y \leqslant 7)$ with 351×351 boxes of dimensions $\Delta x = \Delta y = 0.04$ and use, within each box, four pairs of particles initially separated by a distance $\varepsilon = 0.01$. Figure 12(*b*) shows the result for the case $\lambda = 0.40$ computed after one period of co-rotation. The light and dark regions correspond to high and low values of the direct expansion rate, respectively. This diagnostic markedly identifies the main transport barriers of the flow, i.e. the manifolds of the hyperbolic point H_1. Note, also, that the fluid particles undergoing the highest stretching are located in the regions close to the vortex patches and along the boundaries of the outer recirculation regions. On the contrary, the fluid elements located inside the vortices and within the outer recirculation regions are characterized by small values of the expansion rate, due to the effect of laminar motion and the presence of the elliptic points E_1, E_2, E_3 and E_4 (see figure 4).

5.2. *Stirring*

We quantify the stirring performance of an initially elliptical vortex pair using the mix-norm. The mix-norm (Mathew *et al.* 2005) is a multi-scale measure of the ‘mixedness’ of a concentration field. It is defined as the root mean square of the average values of a zero-mean concentration field over a dense set of subsets contained in the flow domain. The reader is referred to the article by Mathew *et al.* (2005) for a detailed derivation of the mix-norm and to Mathew *et al.* (2007) for an application of the mix-norm to mixing control.

In order to characterize stirring using the mix-norm on a circular domain, we derive the mix-norm in polar coordinates. The derivation, that follows the work by Mathew *et al.* (2005), is not trivial. The reader is referred to the work by Rizzi (2009) for the details. Here, we present only the final result for a given circular domain S^a of radius a and a scalar field $c \in L^2_{S^a}$, for example a concentration field. The mix-norm of the scalar field c on the domain S^a is

$$\Phi(c) = \left[\sum_{n=1}^{\infty} (A_{0,n})^2 \lambda_{0,n} + \sum_{m=1}^{\infty} \sum_{n=1}^{\infty} \left(A^2_{m,n} \; + \; B^2_{m,n} \right) \frac{\lambda_{m,n}}{2} \right]^{1/2}, \tag{5.5}$$

with

$$\lambda_{0,n} = \frac{16a^4\pi}{(\beta_{0,n})^2} [\mathrm{J}_1(\beta_{0,n})]^2 \int_0^a \left[\mathrm{J}_1 \left(\frac{\beta_{0,n}}{2a} \rho \right) \right]^2 \frac{1}{\rho^2} \, \mathrm{d}\rho, \quad m = 0, \tag{5.6}$$

$$A_{0,n} = \frac{\displaystyle\int_0^a \int_{-\pi}^{\pi} c(\rho, \theta) \mathrm{J}_0 \left(\frac{\beta_{0,n}}{a} \rho \right) \; \rho \, \mathrm{d}\rho \, \mathrm{d}\theta}{\pi a^2 \left[\mathrm{J}_1(\beta_{0,n}) \right]^2}, \quad m = 0, \tag{5.7}$$

$$\lambda_{m,n} = \frac{16a^4\pi}{(\beta_{m,n})^2} [\mathrm{J}_{m+1}(\beta_{m,n})]^2 \int_0^a \left[\mathrm{J}_1 \left(\frac{\beta_{m,n}}{2a} \rho \right) \right]^2 \frac{1}{\rho^2} \, \mathrm{d}\rho, \quad \forall \, m \neq 0 \tag{5.8}$$

$$A_{m,n} = \frac{\displaystyle 2 \int_0^a \int_{-\pi}^{\pi} c(\rho, \theta) \mathrm{J}_m \left(\frac{\beta_{m,n}}{a} \rho \right) \cos(m\theta) \; \rho \, \mathrm{d}\rho \, \mathrm{d}\theta}{\pi a^2 \left[\mathrm{J}_{m+1}(\beta_{m,n}) \right]^2}, \quad \forall \, m \neq 0, \tag{5.9}$$

$$B_{m,n} = \frac{\displaystyle 2 \int_0^a \int_{-\pi}^{\pi} c(\rho, \theta) \mathrm{J}_m \left(\frac{\beta_{m,n}}{a} \rho \right) \sin(m\theta) \; \rho \, \mathrm{d}\rho \, \mathrm{d}\theta}{\pi a^2 \left[\mathrm{J}_{m+1}(\beta_{m,n}) \right]^2}, \quad \forall \, m \neq 0, \tag{5.10}$$

where $\mathrm{J}_k(\cdot)$ is the Bessel function of the first kind of order k, $\beta_{k,n}$ is the nth zero of $\mathrm{J}_k(\cdot)$, (ρ, θ) are the polar coordinates and $\lambda_{m,n}$ are the eigenvalues of the so-called mix-operator. The reader is referred to Mathew *et al.* (2005) for a detailed definition of the mix-operator. In general, the mix-norm (5.5) cannot be analytically computed but must be numerically evaluated.

Figure 13 shows the snapshots of the concentration field on a domain of radius $R = 7$ stirred by pairs of elliptic vortices of initial aspect ratios $\lambda = 0.40$, 0.84, 0.8947, at a time corresponding to one period of co-rotation, when starting from the initial conditions $y = 0$, $y = x$, $x = 0$ and $y = -x$. The frame of reference of the figures rotates with the vortex pair. We identify two regions of the domain in which stirring is controlled by different mechanisms: chaotic in the inner core and inner recirculation regions, and laminar in the outer recirculation regions. This distinction is crucial to understand the key role that the geometry of the initial concentration field plays with respect to stirring enhancement.

Stirring confined in the inner core and inner recirculation regions is, after an initial delay related to the orientation of the interface, chaotic. Figure 13 shows that the level of chaotic advection decreases sharply as the initial aspect ratio of the vortices

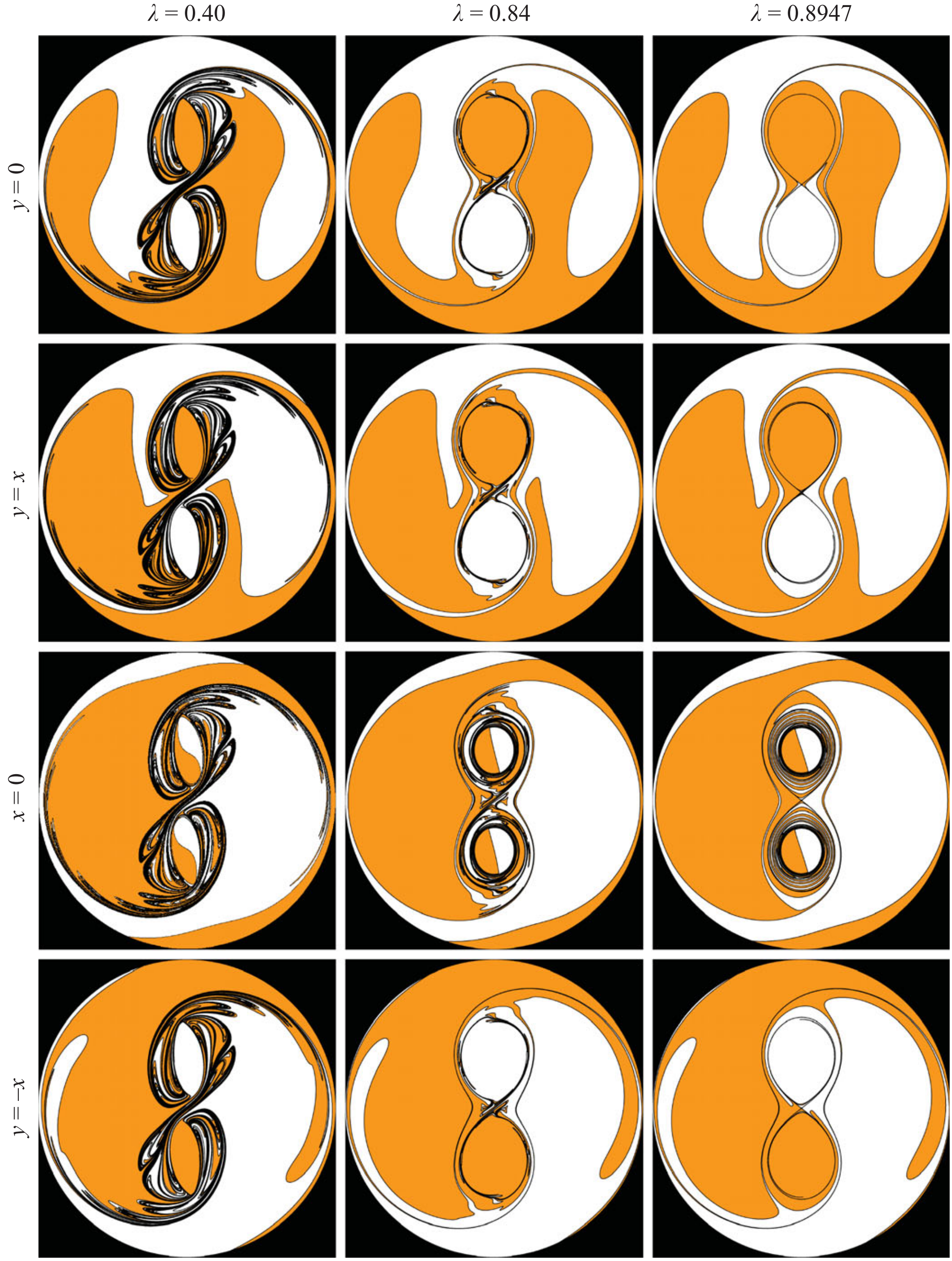

FIGURE 13. (Colour online) Snapshots of the concentration field stirred, over one period of co-rotation, by pairs of vortices of initial aspect ratios $\lambda = 0.40$, 0.84 and 0.8947. The domain has radius $R = 7$ and the initial concentration fields are delimited by the lines $y = 0$, $y = x$, $x = 0$ and $y = -x$. The snapshots are presented in a frame of reference rotating with the vortex pair.

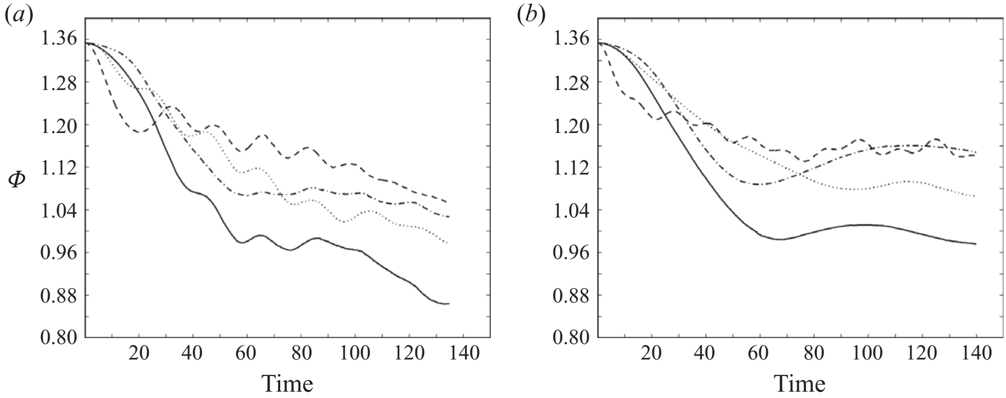

FIGURE 14. Mix-norm, Φ, of the time evolution of the concentration fields initially delimited by the lines $y=0$ (solid line), $y=x$ (dotted), $x=0$ (dashed) and $y=-x$ (dash-dotted), see figure 13. The domain has radius $R=7$ and the initial aspect ratios of the vortices are $\lambda=0.40$ (*a*) and $\lambda=0.84$ (*b*).

becomes greater than 0.80. Stirring in the outer recirculation regions is laminar and is characterized by lobes of fluid whose shape and size strictly depend on the initial orientation of the interface, i.e. on the fraction of grey and white fluids initially contained in the outer recirculation regions, as shown by each column in figure 13. The first row of figure 13 shows that the initial concentration field with the horizontal interface yields to a configuration where the outer recirculation regions are occupied by two lobes of nearly the same extension, filled with different fluids. This is a consequence of the fact that the interface $y=0$ initially crosses the outer recirculation regions and passes through the elliptic points E_3 and E_4, see figure 4. Consequently, the two points of the interface coinciding with E_3 and E_4 are fixed, and the interface is stretched and folded around them by the slow swirling motion induced by the 'ghost' vortices located at the points E_3 and E_4. On the other hand, the initial condition $y=x$ generates single lobes that nearly fill the outer recirculation regions (second row of figure 13), the vertical interface, $x=0$, does not yield to the formation of lobes (third row of figure 13) because, initially, the outer recirculation regions are filled with the same type of fluid and, finally, the initial condition $y=-x$ yields to two thin lobes that occupy only a small area of the outer recirculation regions (fourth row of figure 13).

Figure 14 shows the time evolution of the mix-norm over one period of co-rotation, computed for the four geometries of the initial concentration field and vortices of initial aspect ratios $\lambda=0.40$ and $\lambda=0.84$ (see first and second columns of figure 13). The mix-norm has the same overall trend for both aspect ratios because its value is dominated by the laminar stirring induced in the outer recirculation regions, which occupy 85 % of the domain. Chaotic advection is responsible for the faster decay of the mix-norm in the case $\lambda=0.40$. Note that for a fixed value of the initial aspect ratio, for times up to $t\approx 25$, the mix-norm decreases more rapidly for the initial concentration field with a vertical interface, $x=0$, than the other cases. This is because at time $t=0$ the vertical interface cuts the vortices in half and passes through the elliptic points E_1 and E_2. Consequently, the two points of the interface coinciding with E_1 and E_2 are fixed, and the interface is quickly wrapped into a tight spiral around the vortices forming a fine lamellar structure (see the third row of figure 13). However, for longer times, the initial concentration field with the horizontal interface,

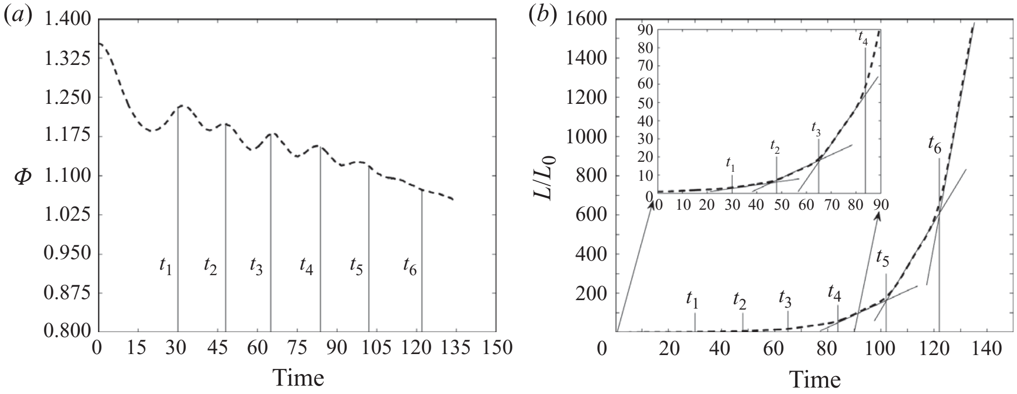

FIGURE 15. Comparison between the mix-norm (*a*) and stretching of the interface (*b*) of a concentration field stirred by a pair of vortices of initial aspect ratio $\lambda = 0.40$. The times $t_1, \ldots, t_6$ correspond to the instants where stretching of the interface changes slope, see (*b*), and the mix-norm has nearly its local maxima, see (*a*). The domain has radius $R = 7$ and the initial concentration field is delimited by the line $x = 0$.

$y = 0$, yields to the best stirring performance. This is in disagreement with the result obtained using stretching of the interface as an indicator for stirring. For the domain $R = 7$, a comparison of the two diagnostics shows that this disagreement is due to the fact that the value of the mix-norm is dominated by the shape and size of the lobes that are created by the laminar flow in the outer recirculation regions, while stretching is dominated by the chaotic flow induced in the inner core and inner recirculation regions.

Interestingly, the mix-norm does not decrease monotonically. There are low- and high-frequency oscillations due to the evolution of the lobes in the outer recirculation regions and to the tangle dynamics, respectively. This seems to conflict with the monotonic evolution of stretching of the interface. However, the local maxima and minima of the high-frequency oscillations of the mix-norm are strongly coupled to the changes of stretching of the interface. This becomes evident by comparing the time evolution of the mix-norm with the stretching of the interface initially vertical, $x = 0$, for a pair of vortices of initial aspect ratio $\lambda = 0.40$. In this case, there are no low-frequency oscillations because no lobes are formed in the outer recirculation region. Figure 15(*a*) shows that the local maxima of the mix-norm occur at about the instants of time when stretching of the interface changes slope, see figure 15(*b*).

The non-monotonic behaviour of the mix-norm can be explained by analysing, as an example, how the concentration field evolves during the time interval between the first and second changes of slope of the stretching of the interface, i.e. between times $t_1 = 30.05$ and $t_2 = 48.05$, see figure 15(*b*). To this end, we divide the interval $[t_1, t_2]$ into five equal subintervals delimited by the time values: $\tau_1 \equiv t_1 = 30.05$, $\tau_2 = 33.65$, $\tau_3 = 37.25$, $\tau_4 = 40.85$, $\tau_5 = 44.45$, $\tau_6 \equiv t_2 = 48.05$. The corresponding snapshots of the concentration fields are presented in figure 16, which shows two different phases of the evolution of the concentration field. During the first phase (τ_1, τ_4), depicted in figures 16(*a–d*), the fluid elements located in the region near the saddle point, H_1, experience a continuous stretching along the unstable manifold, and this is reflected by a drop in the mix-norm which reaches its local minimum at $\tau_4 = 40.85$. During the second phase (τ_4, τ_6), depicted in figures 16(*d–f*), the fluid elements located in

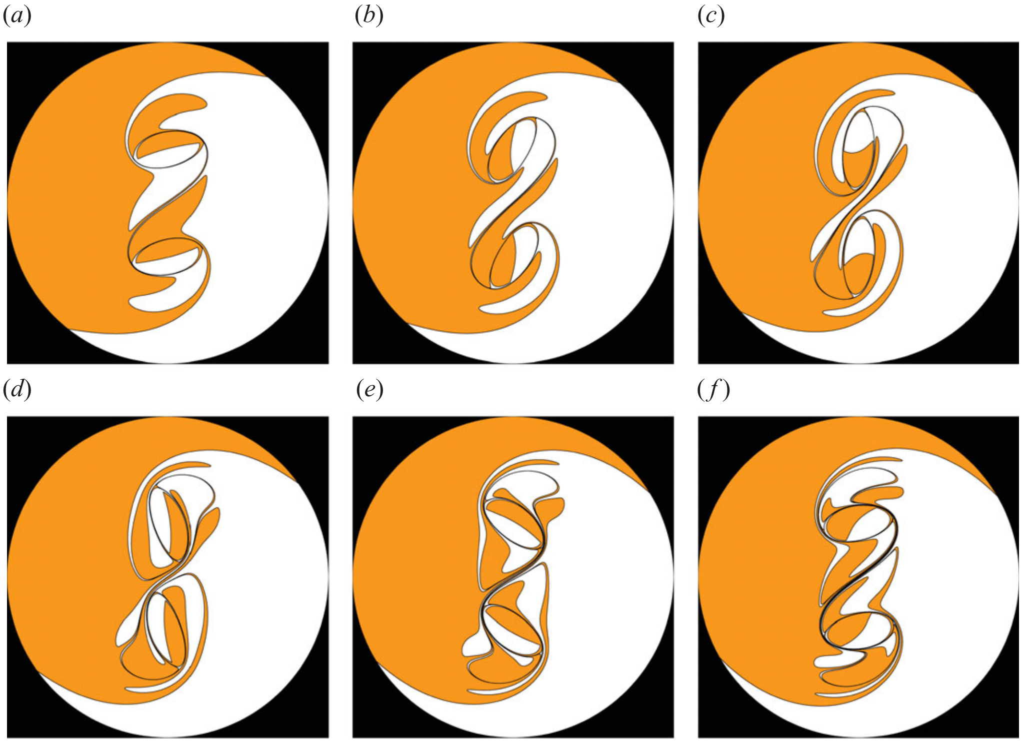

FIGURE 16. (Colour online) Snapshots at times $t = 30.05$ (*a*), 33.65 (*b*), 37.25 (*c*), 40.85 (*d*), 44.45 (*e*) and 48.05 (*f*) of the concentration field stirred by a pair of vortices of initial aspect ratio $\lambda = 0.40$. The domain has radius $R = 7$ and the initial concentration field is delimited by the line $x = 0$. The snapshots are presented in a frame of reference rotating with the vortex pair.

the region around the saddle point undergo to a continuous folding, which spreads the lamellae around the saddle point H_1, and this is reflected by an increase in the mix-norm. This also explains the piecewise trend of the stretching of the interface, see figure 15(*b*). Stretching is linear during the interval (τ_1, τ_4) and changes slope during the folding phase (τ_4, τ_6). This mechanism of stretching and folding repeats itself periodically in time over each half-period of rotation and seems to be responsible for the non-monotonic behaviour of the mix-norm and for the change of the slope of stretching of the interface, see figure 15.

Figure 17 shows the snapshots of the concentration field advected on a domain of radius $R = 0.5$ by pairs of vortices of initial aspect ratios $\lambda = 0.40$, 0.84, 0.8947, after one period of co-rotation, when starting from the initial conditions $y = 0$, $y = x$, $x = 0$ and $y = -x$. The figures are presented in a frame of reference rotating with the vortex pair. Note that for domains of this size, i.e. domains with radius small with respect to the half-separation of the centroids, the flow is dominated by the dynamics of the saddle point H_1, while the dynamics of the other fixed points (E_1, E_2, E_3, E_4, H_2 and H_3) have a negligible effect, see figure 4. The concentration field is increasingly better stirred, i.e. has an exponentially larger number of lamellae, as the initial aspect ratio decreases from 0.8947 to 0.40, since the unstable and stable manifolds of the saddle point H_1 undergo to deformations in time whose amplitude increases greatly as the aspect ratio decreases. Figure 18 shows the time evolution of the corresponding

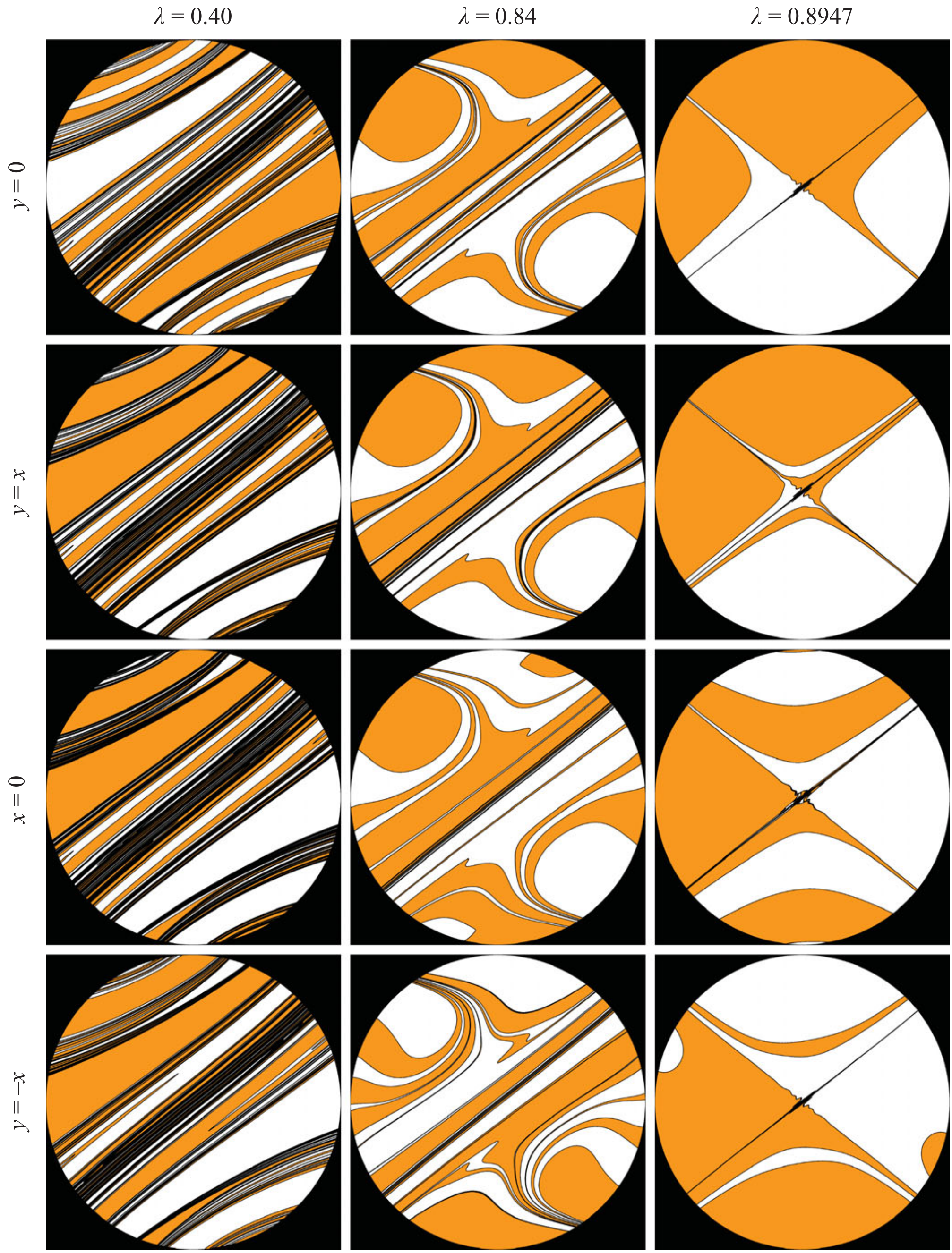

FIGURE 17. (Colour online) Snapshots of the concentration field stirred, over one period of co-rotation, by pairs of vortices of initial aspect ratios $\lambda = 0.40$, 0.84 and 0.8947. The domain has radius $R = 0.5$ and the initial concentration fields are delimited by the lines $y = 0$, $y = x$, $x = 0$ and $y = -x$. The snapshots are presented in a frame of reference rotating with the vortex pair.

mix-norms. The mix-norm presents, in all cases, large and frequent fluctuations due to the transport of fluid in and out of the domain. New thick lamellae enter the domain due to the folding action of the vortices, while the old lamellae become

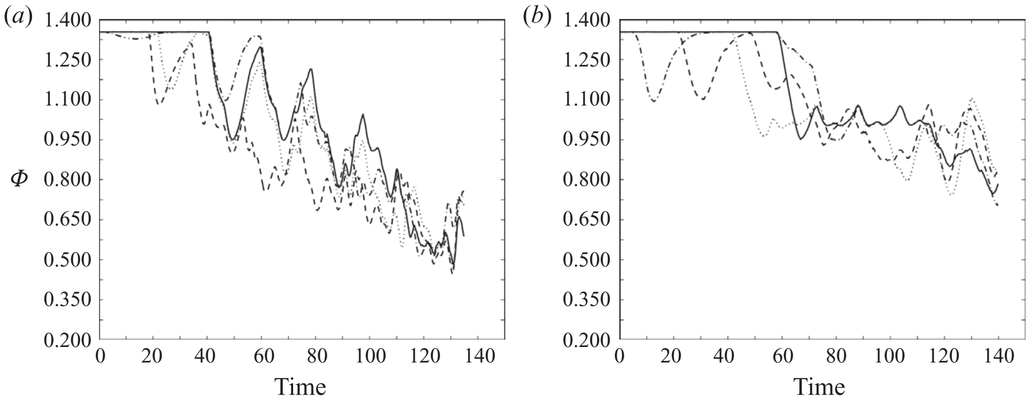

FIGURE 18. Mix-norm, $\varPhi$, of the time evolution of the concentration fields initially delimited by the lines $y=0$ (solid line), $y=x$ (dotted), $x=0$ (dashed) and $y=-x$ (dash-dotted), see figure 17. The domain has radius $R=0.5$ and the initial aspect ratios of the vortices are $\lambda=0.40$ (*a*) and $\lambda=0.84$ (*b*).

thinner as the fluid is squeezed out of the domain by the stretching action of the vortices. The amplitude and frequency of these oscillations increase as the aspect ratio decreases from 0.8947 to 0.40 because the tangle dynamics becomes more effective. The mix-norm, for a fixed value of the aspect ratio, seems to depend on the geometry of the initial concentration field only at the beginning of the evolution and, after an initial delay, is nearly equivalent in all cases. The stirring performance improves as the aspect ratio decreases from 0.8947 to 0.40 and, after one period of co-rotation, the best stirring performance is induced by vortex pairs with initial aspect ratio $\lambda=0.40$.

Figure 19 shows the snapshots of the concentration field with initial interface $y=0$, advected on a domain of radius $R=20$ by pairs of vortices of initial aspect ratio $\lambda=0.40$, 0.84, 0.8947, during one period of co-rotation, at times corresponding to co-rotation angles $\alpha=\pi/2$, π, $3\pi/2$, 2π. The figures are presented in a frame of reference rotating with the vortex pair. For the sake of clarity, we omit the snapshots for the other initial concentrations fields ($y=x$, $x=0$ and $y=-x$) because they yield to similar conclusions. Note that the details of the chaotic flow around the saddle point H_1 are negligible because the system is dominated by the outer flow and, in minor part, by the flow in outer recirculation regions. Figure 20 shows the time evolution of the corresponding mix-norm. The mix-norm is nearly the same in all cases during the first half of the evolution. The different initial aspect ratio of the vortices slightly affects the mix-norm during the second half of the evolution. Overall, the geometrical details of the vortices and the orientation of the initial concentration field have negligible impact, and stirring is mainly dominated by the outer flow.

5.3. *Dependence of stretching and stirring on the angular impulse*

To characterize the effects of the angular impulse, σ, we consider a vortex pair of initial aspect ratio $\lambda=0.60$ and vary σ in the range $10\leqslant\sigma\leqslant 39$. We compute the time evolution of the concentration field initially delimited by the line $y=0$. As shown in § 5 for $\sigma=24.4$, this initial concentration field yields the lowest value of the mix-norm after one period of co-rotation, regardless of the choice of the aspect ratio.

Since the nominal domain is unbounded, we need to choose a finite-size domain that allows us to perform a fair comparison of the stirring and stretching induced by vortex pairs with different angular impulse. We choose a circular domain of

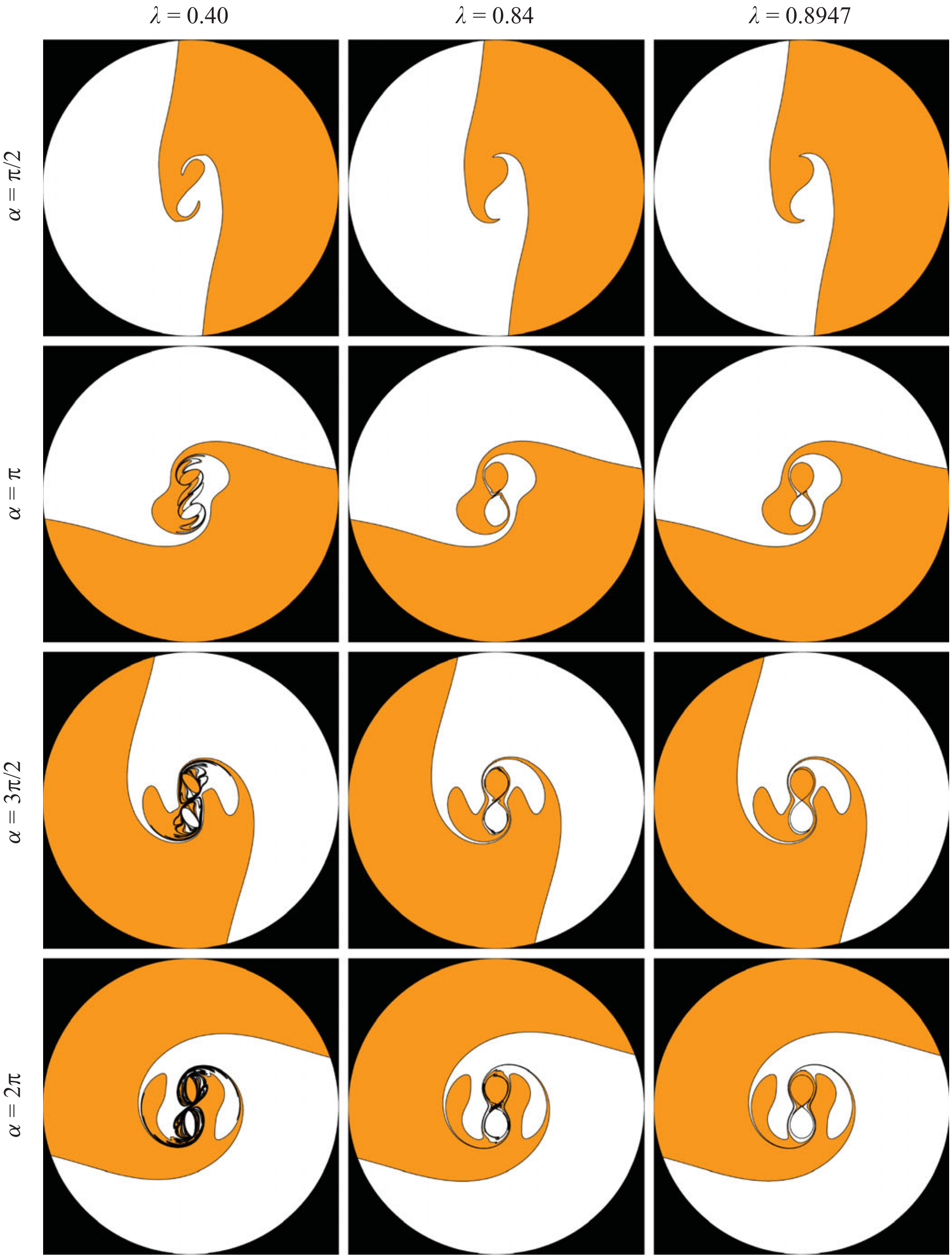

FIGURE 19. (Colour online) Snapshots, at times corresponding to the co-rotation angles $\alpha = \pi/2$, $\alpha = \pi$, $\alpha = 3\pi/2$ and $\alpha = 2\pi$, of the concentration field with the interface initially oriented horizontally, $y = 0$, advected by pairs of vortices of initial aspect ratios $\lambda = 0.40$, 0.84, 0.8947 on a domain of radius $R = 20$. The figures are presented in a frame of reference rotating with the vortex pair.

dimensionless radius $R = 9$ because this is the smallest radius for which the transport of fluid in and out of the domain is minimal for all cases. This domain nearly encloses the outer separatrices of the vortex pair with the largest angular impulse considered,

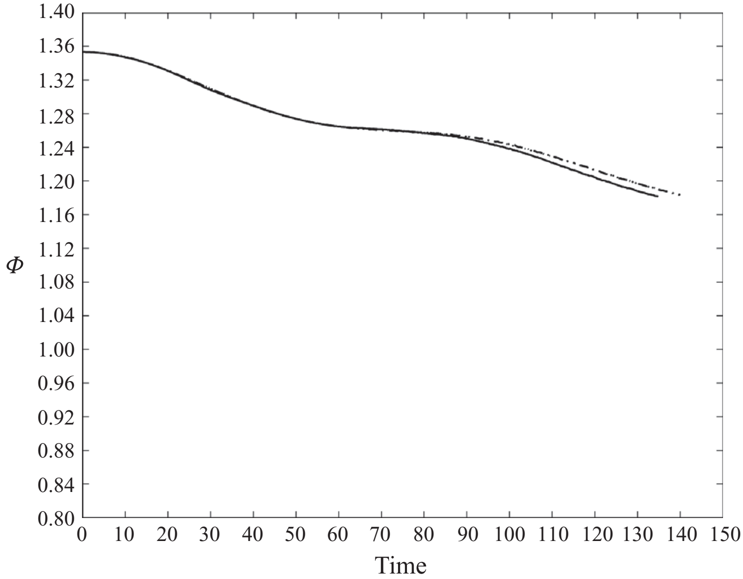

FIGURE 20. Mix-norm, Φ, of the time evolution of the concentration field initially delimited by the line $y = 0$, stirred by vortices of initial aspect ratios $\lambda = 0.40$ (solid line), 0.84 (dash-dotted) and 0.8947 (dotted), see figure 19. The domain has radius $R = 20$.

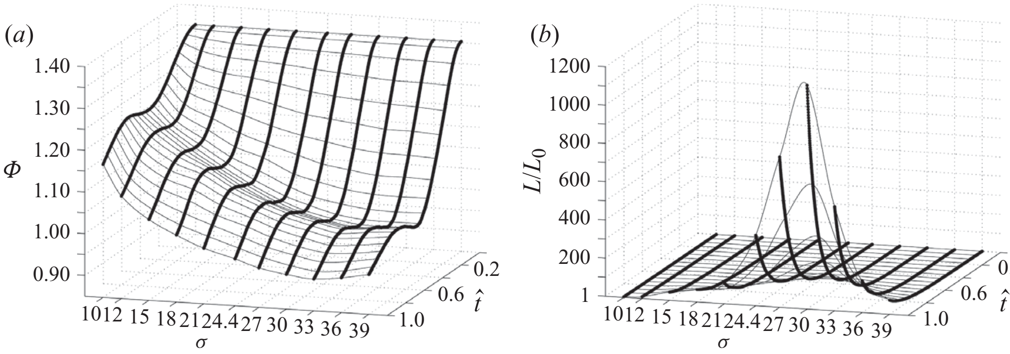

FIGURE 21. Three-dimensional plots of the mix-norm (*a*) and stretching of the interface (*b*) as a function of σ and the normalized time, $\hat{t}$, for the time evolution of a concentration field stirred by a pair of vortices of initial aspect ratio $\lambda = 0.60$ and angular impulses $\sigma = 10$, 12, 15, 18, 21, 24.4, 27, 30, 33, 36 and 39. The domain has radius $R = 9$ and the initial concentration field is delimited by the line $y = 0$. The thin lines represent the cubic interpolation of the data computed (thick lines).

$\sigma = 39$. Since the period of co-rotation of two like-signed vortices increases as the angular impulse σ increases, a normalized time, $\hat{t}$, is defined in order to compare the cases considered. For a given σ, we define $\hat{t}$ as the ratio between the time t and the period of co-rotation.

Figure 21(*a*–*b*) shows the three-dimensional plots of the mix-norm and stretching of the interface L/L_0, as a function of σ and the normalized time, $\hat{t}$. The thin lines are the cubic spline interpolations of the data computed for a vortex pair of initial aspect ratio $\lambda = 0.60$ and angular impulse $\sigma = 10$, 12, 15, 18, 21, 24.4, 27, 30, 33,

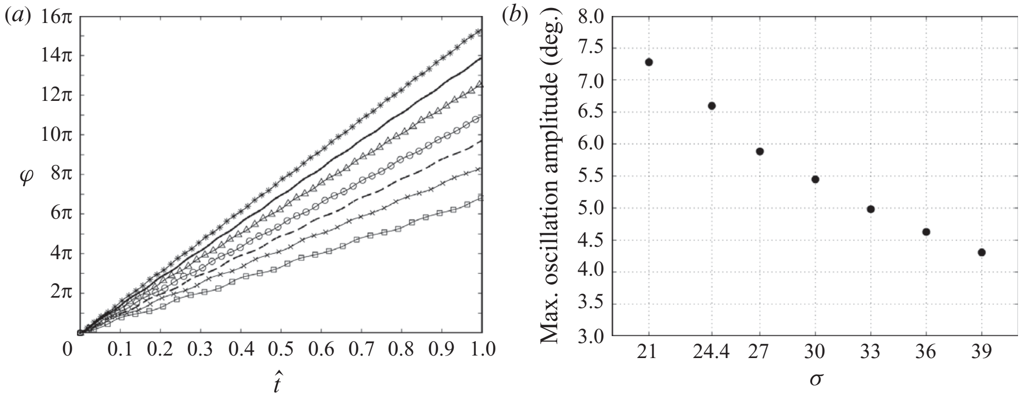

FIGURE 22. (a) Rotation angle φ as a function of the normalized time $\hat{t}$ computed for the vortex pairs of aspect ratio $\lambda = 0.60$ and angular impulses $\sigma = 21$ (□), 24.4 (×), 27 (dashed), 30 (○), 33 (△), 36 (solid) and 39 (∗). (b) Maximum amplitude of oscillation in degrees of the eigendirections of the stable and unstable manifolds of the hyperbolic point at the joint centre of co-rotation, H_1, as a function of the angular impulse.

36 and 39. Figure 23 presents the associated snapshots of the concentration field after one period of co-rotation, in a frame of reference rotating with the vortex pair.

Figure 21 shows that for $\sigma = 10$ the time evolution of the mix-norm reaches its maximum, while stretching reaches its minimum. These diagnostics indicate a poor degree of stirring. The snapshot of the corresponding concentration field (figure 23a) shows that the vortices quickly merge, leading to a single elliptic vortex with long filaments undergoing roll-up and instabilities near the end. In this case, the degree of stirring is minimal because the hyperbolic point H_1 is lost and, with it, the mechanism responsible for stretching and folding described in § 5.2. As σ increases from 10 to 30, the mix-norm decreases while stretching increases, indicating that the stirring performance of the system improves significantly, see figure 21. The mix-norm presents a minimum at $\sigma \approx 33$, while stretching has a sharp maximum at $\sigma \approx 30$. For values of $\sigma > 33$, the mix-norm mildly increases and stretching quickly decreases.

The extrema of the diagnostics indicate that for a circular domain of radius $R = 9$, the best stirring performance is obtained for a value of the angular impulse in the range $30 \leqslant \sigma \leqslant 33$. Apparently, this superior stirring performance is induced by two competing mechanisms. On the one hand, the rotation angular velocity of the vortices increases as the angular impulse increases, see figure 22(a). On the other hand, the amplitude of the oscillations of the eigendirections of the stable and unstable manifolds at the joint centre of vorticity decreases as σ increases, see figure 22(b). We envision that for $30 \leqslant \sigma \leqslant 33$, the oscillations of the eigendirections of the manifolds corresponding to the saddle point at the joint centre of vorticity are sufficiently strong to induce a complex tangle and, at the same time, the angular velocity of rotation of the vortices is sufficiently high to wrap the interface in a tight spool around the patches, see figures 23(h) and 23(i). As a consequence, the number of lamellae and the stretching of the interface increases exponentially inducing a minimum in the mix-norm and a maximum in stretching of the interface. For values of σ smaller than 30, the oscillations of the eigendirections of the manifolds are larger but the angular velocity of the vortices is too low to efficiently wrap the interface around the patches,

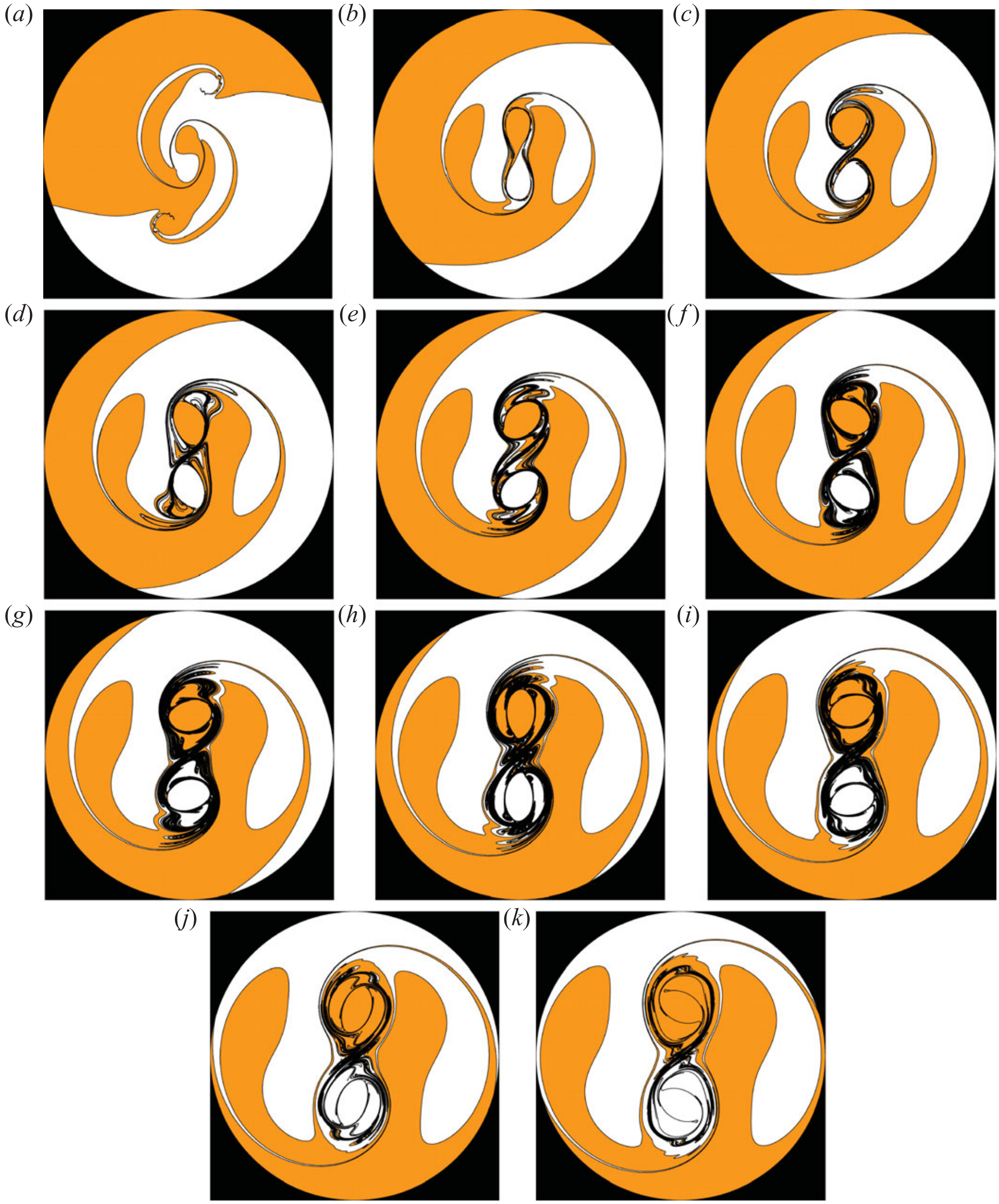

FIGURE 23. (Colour online) Snapshots of the concentration field stirred, over one period of co-rotation, by a pair of vortices of initial aspect ratio $\lambda = 0.60$ and angular impulses $\sigma = 10$ (*a*), 12 (*b*), 15 (*c*), 18 (*d*), 21 (*e*), 24.4 (*f*), 27 (*g*), 30 (*h*), 33 (*i*), 36 (*j*) and 39 (*k*). The domain has radius $R = 9$ and the initial concentration field is delimited by the line $y = 0$. The snapshots are presented in a frame of reference rotating with the vortex pair.

see figures 23(*a*–*g*). For values of σ larger than 33, although the angular velocity of rotation is higher, the oscillations of the eigendirections of the manifolds are too weak to generate a tangle complex enough to be efficiently wrapped around the vortices, figure 23(*j*–*k*).

6. Summary and conclusions

In this study, we characterized transport, stretching and stirring generated by a pair of like-signed initially elliptical identical vortex patches with a uniform vorticity distribution, embedded in an incompressible inviscid fluid occupying a two-dimensional infinite domain.

We showed that the dynamics of a pair of like-signed vortices is determined by the initial value of the aspect ratio, λ, of their elliptical shape. For a given angular impulse $\sigma = 24.4$, if the initial aspect ratio is less than 0.40, the patches rapidly deform and begin merging. Over one period of co-rotation, if $0.40 \leqslant \lambda < 0.80$, the vortices rotate around themselves while co-rotating around the joint centre of vorticity describing, therefore, open trajectories in the phase portrait. If $0.80 \leqslant \lambda \leqslant 0.8947$, the shape of the patches oscillates around its initial orientation while the vortices co-rotate around the joint centre of vorticity describing closed trajectories in the phase portrait.

We characterized the dynamics of the vortex system in terms of fixed points and separatrices. The latter divide the fluid domain into the inner core, inner recirculation and outer recirculation regions, and outer flow. Transport within these regions is regulated by the rotational and co-rotational motion of the vortices which perturb the separatrices. We identified two regimes. When the shape of the vortices oscillates about its initial orientation, i.e. their aspect ratio is $0.80 \leqslant \lambda \leqslant 0.8947$, the induced perturbations are weak and the separatrices undergo to small deformations leading to minimal stirring and transport. When, instead, the vortices rotate around themselves, i.e. $0.40 \leqslant \lambda < 0.80$, the perturbations become stronger as λ decreases and substantially alter the geometry of the separatrices creating a complicated tangle characterized by lobes. New lobes form and develop every half a period of rotation. Transport is very efficient between the inner core and inner recirculation regions, while only a small amount of fluid from the outer recirculation regions is entrained. Transport in and out the outer flow is inhibited by the presence of the outer separatrices which remain nearly unperturbed for all values of the aspect ratio λ.

We quantified stretching and stirring on three circular sub-domains of dimensionless radii $R = 0.5$, 7 and 20. The domain of radius $R = 7$, which nearly contains the area delimited by the outer separatrices, is the sub-domain that we consider as the most appropriate for characterizing the performance of the vortex system. Since stretching and stirring depend on the initial configuration of the scalar field, we considered four simple configurations of the initial scalar field, where two uniform concentrations are separated by a straight-line interface of different orientations. On the sub-domain of radius $R = 0.5$, we quantified stretching in terms of the time evolution of the number of lamellae because segments of the interface were continuously transported in and out the domain. In this case, stretching is dominated by the dynamics of the saddle point located at the joint centre of vorticity, the centre of the domain. The number of lamellae grows exponentially with time for all the aspect ratios considered, and the value of the exponent increases as the aspect ratio decreases. For the case $R = 7$, when the domain encloses almost exactly the outer separatrices, the interface evolves within the domain and its stretching can easily be computed. We showed that stretching depends both on the initial aspect ratio of the vortices and the initial orientation of the interface. Stretching results from the coupling between the rotational and the co-rotational motion of the vortices, and increases as their initial aspect ratio decreases. The time evolution of stretching is piecewise-linear when the vortices rotate around themselves while co-rotating around the joint centre of vorticity, i.e. when $0.40 \leqslant \lambda < 0.80$. The folding phase of the flow is responsible for the change of slope.

For the case $\lambda = 0.40$, the slope of stretching increases by about a factor 3.25 at each half-period of rotation and, therefore, stretching is overall exponential. Stretching is not piecewise-linear when the vortices have an initial aspect ratio greater than 0.80, i.e. when the shape of the patches simply oscillates around their initial orientation. The results for the case $R = 20$ are similar to those for $R = 7$, but the stretching of the interface is reduced because a large part of the interface lies in regions where laminar transport dominates. The initial orientation of the interface plays, also, a key role on stretching. We found that regardless of the initial value of the aspect ratio, among all the orientations considered, the interfaces that initially cross the elliptic points at the centre of the 'ghost vortices' and the elliptic points at the centre of the vortex patches undergo to the lowest and highest degree of stretching, respectively.

The analysis of stretching over finite time, one period of co-rotation, leads to the conclusion that stirring is chaotic within the inner core and inner recirculation regions, while is laminar within the outer recirculation regions and outer flow. To validate this analysis, we computed the finite-time Lyapunov exponent and the direct expansion rate for the vortex system. The asymptotic value of the finite-time Lyapunov exponent is nearly the same for the range $0.40 \leqslant \lambda < 0.80$, i.e. when the vortices rotate on themselves. This value suddenly drops when the shape of the vortices oscillates around its initial orientation, i.e. when $0.80 \leqslant \lambda \leqslant 0.8947$, confirming a sudden change in the dynamics of the vortex system. The direct expansion rate confirms that the maximum rate of strain of fluid elements is located at the joint centre of vorticity and along its manifolds.

We used the mix-norm as a diagnostic to quantify the stirring performance of the vortex system. Since the nominal system is infinite, we considered sub-domains of different radii. We observed that the mix-norm is very sensitive to the size of the sub-domain considered, making the choice of the sub-domain critical. We showed that the stirring performance of the vortex pair seems properly quantified over the smallest sub-domain that encloses the outer separatrices, i.e. the region of radius $R = 7$. Within this sub-domain, the mix-norm is dominated by the dynamics of the fluid in the outer recirculation regions, where there is the formation and development of lobes whose size and shape depend on the initial orientation of the interface. The initial concentration field with the interface crossing the elliptic points located at the centre of the ghost vortices yields, after one period of co-rotation, to the best degree of stirring.

We found that, in general, the time evolution of the mix-norm does not decrease monotonically. Due to the continuous reconfiguration of the concentration field, the mix-norm presents low- and high-frequency oscillations. The local high-frequency maxima and minima of the mix-norm are related to the changes of slope in the time evolution of the stretching of the interface. During each half-period of rotation of the vortices, the mix-norm firstly decreases, because the fluid elements around the saddle point are being stretched along the unstable manifold; secondly, as stretching ends, the fluid elements around the saddle point undergo to a phase of folding, and the mix-norm increases until the next phase of stretching begins.

We showed that the mix-norm and stretching generate conflicting results. Stretching indicates that the vortex system stirs most effectively the initial concentration field subdivided by an interface which crosses the elliptic points located at the centroids of the vortices, while the mix-norm indicates that the best stirring performance is obtained when the interface crosses the elliptic points located at the centre of the 'ghost vortices'. We also noticed that the mix-norm is very sensitive to the size of the domain, while stretching shows negligible sensitivity. These results reinforce previous

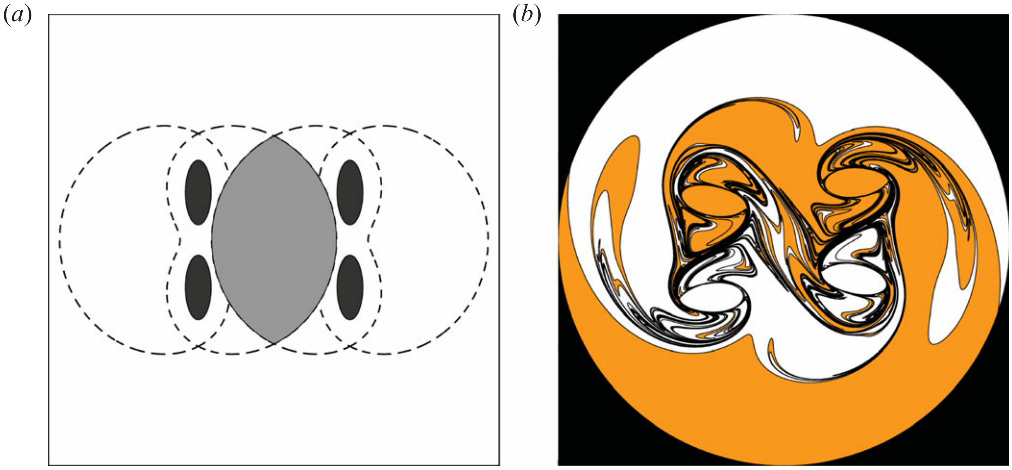

FIGURE 24. (Colour online) (*a*) Initial configuration of two vortex pairs (black) with initial aspect ratio $\lambda = 0.40$, separated by a dimensionless distance $d = 7$. The grey region shows the overlapping of the recirculation regions of the two vortex pairs. (*b*) Snapshot of the concentration field after one period of co-rotation of the vortex pairs. The domain has radius $R = 11$ and the initial concentration field is delimited by the line $y = 0$.

observations that stretching is not a reliable diagnostic of stirring in the cases when stretching is not uniform over the domain, i.e. in most practical cases.

We quantified the effects of the angular impulse, σ, on the stirring performance of the vortex system. For all values of the angular impulse considered, we used the same domain, the smaller subdomain containing the outer separatrices of the vortex system with the highest angular impulse. Surprisingly, stretching presented a sharp maximum at about $\sigma = 30$ indicating a high sensitivity to changes in the angular impulse, while the mix-norm exhibited a weaker minimum at about $\sigma = 33$ indicating a smaller sensitivity. This result indicates that there is an optimal angular impulse which maximizes stretching and minimizes the mix-norm. We argued that this is due to the coupling of two mechanisms: the angular velocity of the vortices, which increases with increasing values of the angular impulse, and the amplitude of oscillations of the eigendirections of the manifolds at the saddle point located at the joint centre of vorticity, which decreases as the angular impulse increases. For $30 \leqslant \sigma \leqslant 33$, the coupling appears to be the most effective.

In conclusion, the vortex system considered does not stir efficiently most of the fluid contained in the outer recirculation regions and the outer flow. This seems to conflict with the experimental evidence that two-dimensional turbulent flows stir very efficiently. The conflict, however, is only apparent in our opinion. We envision that efficient stirring in two-dimensional turbulent flows is mainly generated by the interaction between pairs of vortices with single vortices or with other vortex pairs, interactions that destroy the outer recirculation regions of the vortex pairs and stir the outer fluid. Figure 24 supports this interpretation. For the sake of the argument, we consider two vortex pairs having in common an outer recirculation region and, consequently, bound to interact. The initial concentration field is subdivided by a horizontal interface, $y = 0$, which crosses the elliptic points located at the centre of the 'ghost vortices'. Figure 24 shows that over one period of co-rotation, the fluid contained in the shared outer recirculation region has been stirred due to the interaction between the two vortex pairs.

Funding was provided by NSERC under contract RGPIN217169.

REFERENCES

Aguirre, R. C., Nathman, J. C. & Catrakis, H. C. 2006 Flow geometry effects on the turbulent mixing efficiency. *J. Fluids Engng* **128**, 874–879.

Aref, H. 1984 Stirring by chaotic advection. *J. Fluid Mech.* **143**, 1–21.

Beigie, D., Leonard, A. & Wiggins, S. 1991 Chaotic transport in the homoclinic and heteroclinic tangle regions of quasiperiodically forced two-dimensional dynamical systems. *Nonlinearity* **4**, 775–819.

Beigie, D., Leonard, A. & Wiggins, S. 1994 Invariant manifold templates for chaotic advection. *Chaos, Solitons Fractals* **4**, 749–868.

Cerretelli, C. & Williamson, C. H. K. 2003*a* The physical mechanism for vortex merging. *J. Fluid Mech.* **475**, 41–77.

Cerretelli, C. & Williamson, C. H. K. 2003*b* A new family of uniform vortices related to vortex configurations before merging. *J. Fluid Mech.* **493**, 219–229.

Chakravarthy, V. S. & Ottino, J. M. 1996 Mixing of two viscous fluids in a rectangular cavity. *Chem. Engng Sci.* **51**, 3613–3622.

Deneve, J. A., Fröhlich, J. & Bockhorn, H. 2009 Large eddy simulation of a swirling transverse jet into a crossflow with investigation of scalar transport. *Phys. Fluids* **21** (1), 015101.

Dimotakis, P. E. 2001 Experiments, phenomenology, and simulations of turbulence and turbulent mixing. *APS Meeting Abstracts,* p. 2004.

Dimotakis, P. E. 2005 Turbulent mixing. *Annu. Rev. Fluid Mech.* **37**, 329–356.

Dritschel, D. G. 1985 The stability and energetics of corotating uniform vortices. *J. Fluid Mech.* **157**, 95–134.

Dritschel, D. G. & Zabusky, N. J. 1996 On the nature of vortex interactions and models in unforced nearly-inviscid two-dimensional turbulence. *Phys. Fluids* **8**, 1252–1256.

Eckart, C. 1948 An analysis of the stirring and mixing processes in incompressible fluids. *J. Mar. Res.* **7**, 265–275.

Elhmaidi, D., Provenzale, A. & Babiano, A. 1993 Elementary topology of two-dimensional turbulence from a Lagrangian viewpoint and single-particle dispersion. *J. Fluid Mech.* **257**, 533–558.

Estevadeordal, J. & Kleis, Stanly, J. 2002 Influence of vortex-pairing location on the three-dimensional evolution of plane mixing layers. *J. Fluid Mech.* **462**, 43–77.

Flohr, P. & Vassilicos, J. C. 1997 Accelerated scalar dissipation in a vortex. *J. Fluid Mech.* **348**, 295–317.

Franjione, J. G. & Ottino, J. M. 1987 Feasibility of numerical tracking on material lines and surfaces in chaotic flows. *Phys. Fluids* **30**, 3641–3643.

Fuentes, O. U. V. 2001 Chaotic advection by two interacting finite-area vortices. *Phys. Fluids* **13**, 901–912.

Fuentes, O. U. V. 2005 Vortex filamentation: its onset and its role on axisymmetrization and merger. *Dyn. Atmos. Oceans* **40**, 23–42.

Haller, G. 2001 Distinguished material surfaces and coherent structures in three-dimensional fluid flows. *Physica* D **149** (4), 248–277.

Huang, M.-J. 2005 The physical mechanism of symmetric vortex merger: a new viewpoint. *Phys. Fluids* **17** (7), 074105.

Josserand, C. & Rossi, M. 2007 The merging of two co-rotating vortices: a numerical study. *Eur. J. Mech.* B: *Fluids* **26**, 779–794.

Khakhar, D. V. & Ottino, J. M. 1986 Fluid mixing (stretching) by time periodic sequences for weak flows. *Phys. Fluids* **29**, 3503–3505.

Khakhar, D. V., Rising, H. & Ottino, J. M. 1986 Analysis of chaotic mixing in two model systems. *J. Fluid Mech.* **172**, 419–451.

Le Dizes, S. & Verga, A. 2002 Viscous interactions of two co-rotating vortices before merging. *J. Fluid Mech.* **467**, 389–410.

Leonard, A., Rom-Kedar, V. & Wiggins, S. 1987 Fluid mixing and dynamical systems. *Nucl. Phys.* B. **2**, 179–190.

Leonard, A. D. & Hill, J. C. 1992 Mixing and chemical reaction in sheared and nonsheared homogeneous turbulence. *Fluid Dyn. Res.* **10**, 273–297.

Mathew, G., Mezic, I., Grivopoulos, S., Vaidya, U. & Petzold, L. 2007 Optimal control of mixing in Stokes fluid flows. *J. Fluid Mech.* **580**, 261–281.

Mathew, G., Mezic, I. & Petzold, L. 2005 A multiscale measure for mixing. *Physica* D **211** (1–2), 23–46.

McWilliams, J. C. 1990 The vortices of two-dimensional turbulence. *J. Fluid Mech.* **219**, 361–385.

Melander, M. V., Zabusky, N. J. & McWilliams, J. C. 1988 Symmetric vortex merger in two dimensions: causes and conditions. *J. Fluid Mech.* **195**, 303–340.

Melander, M. V., Zabusky, N. J. & Styczek, A. S. 1986 A moment model for vortex interactions of the two-dimensional euler equations. Part 1. Computational validation of a Hamiltonian elliptical representation. *J. Fluid Mech.* **167**, 95–115.

Meunier, P., Le Dizès, S. & Leweke, T. 2005 Physics of vortex merging. *C. R. Phys.* **6**, 431–450.

Meunier, P. & Villermaux, E. 2003 How vortices mix. *J. Fluid Mech.* **476**, 213–222.

Muzzio, F. J., Swanson, P. D. & Ottino, J. M. 1991 The statistics of stretching and stirring in chaotic flows. *Phys. Fluids* A **3** (5), 822–834.

Nybelen, L. & Paoli, R. 2009 Direct and large-eddy simulations of merging in corotating vortex system. *Am. Inst. Aeronaut. Astronaut. J.* **47**, 157–167.

Ottino, J. M. 1982 Description of mixing with diffusion and reaction in terms of the concept of material surfaces. *J. Fluid Mech.* **114**, 83–103.

Ottino, J. M. 1989 *The Kinematics of Mixing: Stretching, Chaos, and Transport*. Cambridge University Press.

Ottino, J. M. 1990 Mixing, chaotic advection and turbulence. *Annu. Rev. Fluid Mech.* **22**, 207–253.

Padberg, K., Thiere, B., Preis, R. & Dellnitz, M. 2009 Local expansion concepts for detecting transport barriers in dynamical systems. *Commun. Nonlinear Sci. Numer. Simul.* **14**, 4176–4190.

Poje, A. C. & Haller, G. 1999 Geometry of cross-stream Lagrangian mixing in a double gyre ocean model. *J. Phys. Oeanogr.* **29**, 1649–1665.

Pozrikidis, C. 2001 *Fluid Dynamics: Theory, Computation, and Numerical Simulation*. Kluwer.

Provenzale, A. 1999 Transport by coherent barotropic vortices. *Annu. Rev. Fluid Mech.* **31**, 55–93.

Pullin, D. I. 1992 Contour dynamics methods. *Annu. Rev. Fluid Mech.* **24**, 89–115.

Rasmussen, J. J., Nielsen, A. H. & Naulin, V. 2001 Dynamics of vortex interactions in two-dimensional flows. *Phys. Scr.* T **98**, 29–33.

Rizzi, F. 2009 Characterization of stirring generated by a pair of elliptic vortices. Master's thesis, University of Udine, Italy.

Rom-Kedar, V., Leonard, A. & Wiggins, S. 1990 An analytical study of transport, mixing and chaos in an unsteady vortical flow. *J. Fluid Mech.* **214**, 347–394.

Rom-Kedar, V. & Wiggins, S. 1990 Transport in two-dimensional maps. *Arch. Rat. Mech. Anal.* **109**, 239–298.

Rom-Kedar, V. & Wiggins, S. 1991 Transport in two-dimensional maps: concepts, examples, and a comparison of the theory of Rom-Kedar and Wiggins with the Markov model of Mackay, Meiss, Ott and Percival. *Physica* D **51** (1–3), 248–266.

Sau, R. & Mahesh, K. 2007 Passive scalar mixing in vortex rings. *J. Fluid Mech.* **582**, 449–461.

Shadden, S. C., Katija, K., Rosenfeld, M., Marsden, J. E. & Dabiri, J. O. 2007 Transport and stirring induced by vortex formation. *J. Fluid Mech.* **593**, 315–331.

Slessor, M. D., Bond, C. L. & Dimotakis, P. E. 1998 Turbulent shear-layer mixing at high Reynolds numbers: effects of inflow conditions. *J. Fluid Mech.* **376**, 115–138.

Smyth, W. D., Moum, J. N. & Caldwell, D. R. 2001 The efficiency of mixing in turbulent patches: inferences from direct simulations and microstructure observations. *J. Phys. Oceanogr.* **31**, 19691992.

Vainchtein, D. 2005 Private communication.

Vassilicos, J. C. 2002 Mixing in vortical, chaotic and turbulent flows. *Phil. Trans. R. Soc. Lond.* A **360**, 2819–2837.

Villermaux, E. & Duplat, J. 2003 Mixing as an aggregation process. *Phys. Rev. Lett.* **91** (18), 184501.

Von Hardenberg, J., McWilliams, J. C., Provenzale, A., Shchepetkin, A. & Weiss, J. B. 2000 Vortex merging in quasi-geostrophic flows. *J. Fluid Mech.* **412**, 331–353.

Warhaft, Z. 2000 Passive scalars in turbulent flows. *Annu. Rev. Fluid Mech.* **32**, 203–240.

Wiggins, S. 1987 Chaos in the quasiperiodically forced duffing oscillator. *Phys. Lett.* A **124**, 138–142.

Witt, A., Braun, R., Feudel, F., Grebogi, C. & Kurths, J. 1999 Tracer dynamics in a flow of driven vortices. *Phys. Rev.* E **59**, 1605–1614.

Wolf, A., Swift, J. B., Swinney, H. L. & Vastano, J. A. 1985 Determining Lyapunov exponents from a time series. *Physica* D **16**, 285–317.

Yasuda, I. 1997 Two-dimensional asymmetric vortex merger: merger dynamics and critical merger distance. *Dyn. Atmos. Oceans* **26**, 159–181.

Zabusky, N. J., Hughes, M. H. & Roberts, K. V. 1979 Contour dynamics for the Euler equations in two dimensions. *J. Comput. Phys.* **30**, 96–106.